Measurement of *CP* asymmetries and branching fractions in a time-dependent Dalitz analysis of $B^0 \to (\rho\pi)^0$ and a constraint on the quark mixing angle ϕ_2

A. Kusaka,[40] C. C. Wang,[25] I. Adachi,[8] H. Aihara,[40] K. Arinstein,[1] V. Aulchenko,[1] T. Aushev,[12,17] A. M. Bakich,[37]
V. Balagura,[12] E. Barberio,[20] I. Bedny,[1] K. Belous,[11] U. Bitenc,[13] A. Bondar,[1] A. Bozek,[26] M. Bračko,[13,19] T. E. Browder,[7]
P. Chang,[25] Y. Chao,[25] A. Chen,[23] W. T. Chen,[23] B. G. Cheon,[6] R. Chistov,[12] I.-S. Cho,[45] S.-K. Choi,[5] Y. Choi,[36]
J. Dalseno,[20] M. Dash,[44] S. Eidelman,[1] N. Gabyshev,[1] B. Golob,[13,18] J. Haba,[8] K. Hara,[21] K. Hayasaka,[21] H. Hayashii,[22]
M. Hazumi,[8] D. Heffernan,[31] Y. Hoshi,[39] W.-S. Hou,[25] H. J. Hyun,[16] T. Iijima,[21] K. Inami,[21] A. Ishikawa,[33] H. Ishino,[41]
R. Itoh,[8] M. Iwasaki,[40] Y. Iwasaki,[8] D. H. Kah,[16] J. H. Kang,[45] H. Kawai,[2] T. Kawasaki,[28] H. Kichimi,[8] H. O. Kim,[16]
S. K. Kim,[35] Y. J. Kim,[4] K. Kinoshita,[3] S. Korpar,[13,19] P. Križan,[13,18] P. Krokovny,[8] R. Kumar,[32] C. C. Kuo,[23] A. Kuzmin,[1]
Y.-J. Kwon,[45] J. S. Lee,[36] M. J. Lee,[35] S. E. Lee,[35] T. Lesiak,[26] A. Limosani,[20] S.-W. Lin,[25] Y. Liu,[4] D. Liventsev,[12]
F. Mandl,[10] A. Matyja,[26] S. McOnie,[37] T. Medvedeva,[12] K. Miyabayashi,[22] H. Miyake,[31] H. Miyata,[28] Y. Miyazaki,[21]
R. Mizuk,[12] G. R. Moloney,[20] E. Nakano,[30] M. Nakao,[8] S. Nishida,[8] O. Nitoh,[43] S. Noguchi,[22] T. Nozaki,[8] S. Ogawa,[38]
T. Ohshima,[21] S. Okuno,[14] H. Ozaki,[8] G. Pakhlova,[12] C. W. Park,[36] H. Park,[16] L. S. Peak,[37] R. Pestotnik,[13] L. E. Piilonen,[44]
H. Sahoo,[7] Y. Sakai,[8] O. Schneider,[17] C. Schwanda,[10] A. J. Schwartz,[3] K. Senyo,[21] M. E. Sevior,[20] M. Shapkin,[11]
C. P. Shen,[9] H. Shibuya,[38] B. Shwartz,[1] J. B. Singh,[32] A. Somov,[3] S. Stanič,[29] M. Starič,[13] T. Sumiyoshi,[42] S. Suzuki,[33]
S. Y. Suzuki,[8] F. Takasaki,[8] K. Tamai,[8] N. Tamura,[28] M. Tanaka,[8] Y. Teramoto,[30] I. Tikhomirov,[12] K. Trabelsi,[8] S. Uehara,[8]
K. Ueno,[25] T. Uglov,[12] Y. Unno,[6] S. Uno,[8] P. Urquijo,[20] G. Varner,[7] K. E. Varvell,[37] K. Vervink,[17] S. Villa,[17] C. H. Wang,[24]
M.-Z. Wang,[25] P. Wang,[9] X. L. Wang,[9] Y. Watanabe,[14] E. Won,[15] Y. Yamashita,[27] Z. P. Zhang,[34] V. Zhulanov,[1]
A. Zupanc,[13] and O. Zyukova[1]

(Belle Collaboration)

[1]*Budker Institute of Nuclear Physics, Novosibirsk*
[2]*Chiba University, Chiba*
[3]*University of Cincinnati, Cincinnati, Ohio 45221*
[4]*The Graduate University for Advanced Studies, Hayama*
[5]*Gyeongsang National University, Chinju*
[6]*Hanyang University, Seoul*
[7]*University of Hawaii, Honolulu, Hawaii 96822*
[8]*High Energy Accelerator Research Organization (KEK), Tsukuba*
[9]*Institute of High Energy Physics, Chinese Academy of Sciences, Beijing*
[10]*Institute of High Energy Physics, Vienna*
[11]*Institute of High Energy Physics, Protvino*
[12]*Institute for Theoretical and Experimental Physics, Moscow*
[13]*J. Stefan Institute, Ljubljana*
[14]*Kanagawa University, Yokohama*
[15]*Korea University, Seoul*
[16]*Kyungpook National University, Taegu*
[17]*École Polytechnique Fédérale de Lausanne (EPFL), Lausanne*
[18]*University of Ljubljana, Ljubljana*
[19]*University of Maribor, Maribor*
[20]*University of Melbourne, School of Physics, Victoria 3010*
[21]*Nagoya University, Nagoya*
[22]*Nara Women's University, Nara*
[23]*National Central University, Chung-li*
[24]*National United University, Miao Li*
[25]*Department of Physics, National Taiwan University, Taipei*
[26]*H. Niewodniczanski Institute of Nuclear Physics, Krakow*
[27]*Nippon Dental University, Niigata*
[28]*Niigata University, Niigata*
[29]*University of Nova Gorica, Nova Gorica*
[30]*Osaka City University, Osaka*
[31]*Osaka University, Osaka*
[32]*Panjab University, Chandigarh*
[33]*Saga University, Saga*

^{34}*University of Science and Technology of China, Hefei*
^{35}*Seoul National University, Seoul*
^{36}*Sungkyunkwan University, Suwon*
^{37}*University of Sydney, Sydney, New South Wales*
^{38}*Toho University, Funabashi*
^{39}*Tohoku Gakuin University, Tagajo*
^{40}*Department of Physics, University of Tokyo, Tokyo*
^{41}*Tokyo Institute of Technology, Tokyo*
^{42}*Tokyo Metropolitan University, Tokyo*
^{43}*Tokyo University of Agriculture and Technology, Tokyo*
^{44}*Virginia Polytechnic Institute and State University, Blacksburg, Virginia 24061*
^{45}*Yonsei University, Seoul*

We present the results of a time-dependent Dalitz plot analysis of $B^0 \to \pi^+ \pi^- \pi^0$ decays based on a 414 fb^{-1} data sample that contains $449 \times 10^6 B\overline{B}$ pairs. The data were collected on the $\Upsilon(4S)$ resonance with the Belle detector at the KEKB asymmetric energy e^+e^- collider. Combining our analysis with information on charged B decay modes, we perform a full Dalitz and isospin analysis and obtain a constraint on the quark mixing angle ϕ_2, $68° < \phi_2 < 95°$ at the 68.3% confidence level for the ϕ_2 solution consistent with the standard model. A large standard-model–disfavored region also remains. The branching fractions for the decay processes $B^0 \to \rho^\pm(770)\pi^\mp$ and $B^0 \to \rho^0(770)\pi^0$ are measured to be $(22.6 \pm 1.1[\text{stat}] \pm 4.4[\text{syst}]) \times 10^{-6}$ and $(3.0 \pm 0.5[\text{stat}] \pm 0.7[\text{syst}]) \times 10^{-6}$, respectively. These are the first branching fraction measurements of the process $B^0 \to \rho(770)\pi$ with the lowest resonance $\rho(770)$ explicitly separated from the radial excitations.

I. INTRODUCTION

In the standard model (SM), *CP* violation arises from an irreducible complex phase in the Cabibbo-Kobayashi-Maskawa (CKM) matrix [1]. The SM predicts that measurement of a time-dependent *CP* asymmetry between the decay rates of B^0 and $\overline{B}^0$ gives access to the *CP* violating phase in the CKM matrix [2–4]. The angle ϕ_2 of the CKM unitarity triangle can be measured via the tree diagram contribution in $b \to u\overline{u}d$ decay processes, such as $B^0 \to \pi^+\pi^-$, $B^0 \to \rho^\pm\pi^\mp$, or $B^0 \to \rho^+\rho^-$ [5]. In these decay processes, however, contributions from so-called $b \to d$ penguin diagrams could contaminate the measurement of ϕ_2. Snyder and Quinn pointed out that a Dalitz plot analysis of $B^0 \to \rho\pi$, which includes $B^0 \to \rho^+\pi^-$, $B^0 \to \rho^-\pi^+$, and $B^0 \to \rho^0\pi^0$, offers a unique way to determine ϕ_2 without ambiguity. The Dalitz plot analysis takes into account a possible contamination from the penguin contribution [6]. In addition, an isospin analysis [7,8] involving the charged decay modes, $B^+ \to \rho^+\pi^0$ and $B^+ \to \rho^0\pi^+$, provides further improvement of the ϕ_2 determination.

The Belle [9] and *BABAR* [10] Collaborations recently reported the first measurements employing a time-dependent Dalitz plot analysis technique. In this paper we describe the details of the time-dependent Dalitz plot analysis with the Belle detector at the KEKB asymmetric energy e^+e^- collider reported in Ref. [9]. We also present the first measurements of the branching fractions of $B^0 \to \rho^\pm(770)\pi^\mp$ and $B^0 \to \rho^0(770)\pi^0$ decay processes obtained from the Dalitz plot analysis, where the $\rho(770)$ is

separated from radial excitations. These results can be compared with the branching fraction of the process $B^\pm \to \rho^0(770)\pi^\pm$ [11].

A. KEKB and Belle detector

KEKB [12] operates at the $\Upsilon(4S)$ resonance ($\sqrt{s} = 10.58$ GeV) with a peak luminosity that exceeds 1.6×10^{34} cm^{-2} s^{-1}. At KEKB, the $\Upsilon(4S)$ is produced with a Lorentz boost of $\beta\gamma = 0.425$ nearly along the electron beamline (z). Since the B^0 and $\overline{B}^0$ mesons are approximately at rest in the $\Upsilon(4S)$ center-of-mass system (cms), Δt can be determined from the displacement in the z direction, Δz, between the vertices of the two B mesons: $\Delta t \simeq \Delta z/\beta\gamma c$.

The Belle detector is a large-solid-angle magnetic spectrometer that consists of a silicon vertex detector (SVD), a 50-layer central drift chamber (CDC), an array of aerogel threshold Čerenkov counters (ACC), a barrel-like arrangement of time-of-flight scintillation counters (TOF), and an electromagnetic calorimeter comprised of CsI(Tl) crystals (ECL) located inside a superconducting solenoid coil that provides a 1.5 T magnetic field. An iron flux return located outside of the coil is instrumented to detect K_L^0 mesons and to identify muons (KLM). The detector is described in detail elsewhere [13]. Two inner detector configurations were used. A 2.0 cm beam pipe and a 3-layer silicon vertex detector were used for the first data sample of $152 \times 10^6 B\overline{B}$ pairs (DS-I), while a 1.5 cm beam pipe, a 4-layer silicon detector, and a small-cell inner drift chamber were used to record the remaining $297 \times 10^6 B\overline{B}$ pairs (DS-II) [14].

B. Outline of the analysis

The analysis proceeds in the following steps. First, we extract the signal fraction (Sec. II). We then determine the sizes and phases of the contributions from radial excitations (Sec. III). Using the parameters determined in the steps above, we perform a time-dependent Dalitz plot analysis (Secs. IV, V, and VI). The fit results are interpreted as quasi-two-body *CP* violation parameters (Sec. VII) and as branching fractions of $B^0 \to \rho^{\pm}(770)\pi^{\mp}$ and $B^0 \to \rho^0(770)\pi^0$ decays (Sec. VIII). We subsequently use these results to constrain the CKM angle ϕ_2 (Sec. IX).

C. Differential decay width of time-dependent Dalitz plot

We measure the decay process $B^0 \to \pi^+\pi^-\pi^0$, where we denote the four-momenta of the π^+, π^-, and π^0 by p_+, p_-, and p_0, respectively. The invariant-mass squared of their combinations,

$$s_+ = (p_+ + p_0)^2, \qquad s_- = (p_- + p_0)^2,$$
$$s_0 = (p_+ + p_-)^2, \tag{1}$$

satisfies the following equation:

$$s_+ + s_- + s_0 = m_{B^0}^2 + 2m_{\pi^+}^2 + m_{\pi^0}^2, \tag{2}$$

by energy and momentum conservation. The differential (time-integrated) decay width with respect to the variables above (Dalitz plot) is

$$d\Gamma = \frac{1}{(2\pi)^3} \frac{|\overset{(-)}{A}_{3\pi}|^2}{8m_{B^0}^2} ds_+ ds_-, \tag{3}$$

where $\overset{(-)}{A}_{3\pi}$ is the Lorentz-invariant amplitude of the $B^0(\overline{B}^0) \to \pi^+\pi^-\pi^0$ decay.

In the decay chain $\Upsilon(4S) \to B^0\overline{B}^0 \to f_1 f_2$, where one of the B's decays into final state f_1 at time t_1 and the other decays into another final state f_2 at time t_2, the time-dependent amplitude is

$$A(t_1, t_2) \sim e^{-(\Gamma/2 + iM)(t_1 + t_2)}$$
$$\times \Big\{ \cos[\Delta m_d(t_1 - t_2)/2](A_1\overline{A}_2 - \overline{A}_1 A_2)$$
$$- i\sin[\Delta m_d(t_1 - t_2)/2]\Big(\frac{p}{q}A_1 A_2 - \frac{q}{p}\overline{A}_1\overline{A}_2\Big)\Big\}. \tag{4}$$

Here, p and q define the mass eigenstates of neutral B mesons as $pB^0 \pm q\overline{B}^0$, with average mass M and width Γ, and mass difference Δm_d. The width difference is assumed to be zero.

The decay amplitudes are defined as follows,

$$A_1 \equiv A(B^0 \to f_1), \tag{5}$$

$$\overline{A}_1 \equiv A(\overline{B}^0 \to f_1), \tag{6}$$

$$A_2 \equiv A(B^0 \to f_2), \tag{7}$$

$$\overline{A}_2 \equiv A(\overline{B}^0 \to f_2). \tag{8}$$

In this analysis, we take $A_{3\pi}$ as A_1 and choose f_2 to be a flavor eigenstate, i.e., $A_2 = 0$ or $\overline{A}_2 = 0$. Here we call the B decaying into $f_1 = f_{CP} = \pi^+\pi^-\pi^0$ the *CP* side B, while the other B is the tag-side B, $f_2 = f_{\text{tag}}(\overline{f}_{\text{tag}})$. The differential decay width dependence on time difference $\Delta t \equiv t_{CP} - t_{\text{tag}}$ is then

$$d\Gamma \sim e^{-\Gamma|\Delta t|}\Big\{ (|A_{3\pi}|^2 + |\overline{A}_{3\pi}|^2)$$
$$- q_{\text{tag}} \cdot (|A_{3\pi}|^2 - |\overline{A}_{3\pi}|^2) \cos(\Delta m_d \Delta t)$$
$$+ q_{\text{tag}} \cdot 2\,\text{Im}\Big(\frac{q}{p}A_{3\pi}^*\overline{A}_{3\pi}\Big)\sin(\Delta m_d \Delta t)\Big\} d\Delta t, \tag{9}$$

where we assume $|q/p| = 1$ (*CP* and *CPT* conservation in mixing) and $|A(B^0 \to f_{\text{tag}})| = |A(\overline{B}^0 \to \overline{f}_{\text{tag}})|$, and integrate over $t_{\text{sum}} = t_{CP} + t_{\text{tag}}$. Here q_{tag} is the b-flavor charge, and $q_{\text{tag}} = +1(-1)$ when the tag-side B decays as a B^0 ($\overline{B}^0$) flavor eigenstate.

Combining the Dalitz plot decay width (3) and the time-dependent decay width (9), we obtain the time-dependent Dalitz plot decay width

$$d\Gamma \sim |A(\Delta t; s_+, s_-)|^2 d\Delta t\, ds_+\, ds_-, \tag{10}$$

where

$$|A(\Delta t; s_+, s_-)|^2 = e^{-\Gamma|\Delta t|}\Big\{ (|A_{3\pi}|^2 + |\overline{A}_{3\pi}|^2)$$
$$- q_{\text{tag}} \cdot (|A_{3\pi}|^2 - |\overline{A}_{3\pi}|^2) \cos(\Delta m_d \Delta t)$$
$$+ q_{\text{tag}} \cdot 2\,\text{Im}\Big(\frac{q}{p}A_{3\pi}^*\overline{A}_{3\pi}\Big)\sin(\Delta m_d \Delta t)\Big\}, \tag{11}$$

$$A_{3\pi} = A_{3\pi}(s_+, s_-), \qquad \overline{A}_{3\pi} = \overline{A}_{3\pi}(s_+, s_-). \tag{12}$$

We assume that the $B^0 \to \pi^+\pi^-\pi^0$ decay is dominated by the $B^0 \to (\rho\pi)^0$ amplitudes: $B^0 \to \rho^+\pi^-$, $B^0 \to \rho^-\pi^+$, and $B^0 \to \rho^0\pi^0$, where ρ can be $\rho(770)$, $\rho(1450)$, or $\rho(1700)$. Although there could exist contributions from B^0 decays into non-$\rho\pi$ $\pi^+\pi^-\pi^0$ final states, such as $f_0(980)\pi^0$, $f_0(600)\pi^0$, $\omega\pi^0$, and nonresonant $\pi^+\pi^-\pi^0$, we confirm that these contributions are small; their effects are taken into account as systematic uncertainties (Sec. VI E). The Dalitz plot amplitude $A_{3\pi}(s_+, s_-)$ can then be written as

$$A_{3\pi}(s_+, s_-) = \sum_{\kappa=(+,-,0)} f_\kappa(s_+, s_-)A^\kappa, \tag{13}$$

$$\frac{q}{p}\overline{A}_{3\pi}(s_+, s_-) = \sum_{\kappa=(+,-,0)} \overline{f}_\kappa(s_+, s_-)\overline{A}^\kappa, \qquad (14)$$

where $A^\kappa(\overline{A}^\kappa)$ are complex amplitudes corresponding to $B^0(\overline{B}^0) \to \rho^+\pi^-,\ \rho^-\pi^+,\ \rho^0\pi^0$ for $\kappa = +, -, 0$ and the functions $f_\kappa(s_+, s_-)$ incorporate the kinematic and dynamical properties of the B^0 decay into a vector ρ and a pseudoscalar π. The goal of this analysis is to measure the complex amplitudes A^+, A^-, A^0, $\overline{A}^+$, $\overline{A}^-$, and $\overline{A}^0$; we then constrain the CKM angle ϕ_2 using these amplitudes.

In contrast to a quasi-two-body *CP* violation analysis, the time-dependent Dalitz analysis includes measurements of the sizes of the interferences among the final states $\rho^+\pi^-$, $\rho^-\pi^+$, and $\rho^0\pi^0$, and *CP*-violating asymmetries in the mixed final states. In principle, these measurements allow us to determine all the relative sizes and phases of the amplitudes A^κ and $\overline{A}^\kappa$, which are related to ϕ_2 through an isospin relation [7,8] by

$$e^{+2i\phi_2} = \frac{\overline{A}^+ + \overline{A}^- + 2\overline{A}^0}{A^+ + A^- + 2A^0}. \qquad (15)$$

Consequently, in the limit of high statistics, we can constrain ϕ_2 without discrete ambiguities.

D. Kinematics of $B^0 \to (\rho\pi)^0$

The function $\overset{(-)}{f}_\kappa(s_+, s_-)$ can be factorized into two parts as

$$\overset{(-)}{f}_\kappa(s_+, s_-) = T_J^\kappa F_\pi(s_\kappa) \qquad (\kappa = +, -, 0), \qquad (16)$$

where $F_\pi(s_\kappa)$ and T_J^κ correspond to the line shape of the ρ and the helicity distribution of the ρ, respectively. Here we assume that a single unique functional form for the line shape $F_\pi(s)$ can be used for all six $\overset{(-)}{f}_\kappa$ [15]. Since this assumption has no good theoretical or experimental foundation, we check the validity of the assumption with data and assign systematic errors.

The line shape is parametrized with Breit-Wigner functions corresponding to the $\rho(770)$, $\rho(1450)$, and $\rho(1700)$ resonances:

$$F_\pi(s) = \mathrm{BW}^{\mathrm{GS}}_{\rho(770)} + \beta \cdot \mathrm{BW}^{\mathrm{GS}}_{\rho(1450)} + \gamma \cdot \mathrm{BW}^{\mathrm{GS}}_{\rho(1700)}, \qquad (17)$$

where the amplitudes β and γ (denoting the relative size of two resonances) are complex numbers. We use the Gounaris-Sakurai (GS) model [16] for the Breit-Wigner shape of each resonance [17].

In the case of a pseudoscalar-vector ($J = 1$) decay, T_J^κ is given by

$$T_1^\kappa = -4|\vec{p}_j||\vec{p}_k|\cos\theta^{jk}, \qquad (18)$$
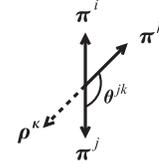
FIG. 1.   The relation between three pions in the rest frame of ρ^κ.

$$\begin{pmatrix} T_1^+ &= -4|\vec{p}_+||\vec{p}_-|\cos\theta^{+-} \\ T_1^- &= -4|\vec{p}_0||\vec{p}_+|\cos\theta^{0+} \\ T_1^0 &= -4|\vec{p}_-||\vec{p}_0|\cos\theta^{-0} \end{pmatrix}, \qquad (19)$$

where $\vec{p}_j$, $\vec{p}_k$ are the three-momenta of the π^j and π^k in the rest frame of ρ^κ (or the $\pi^i\pi^j$ system), and $\theta^{jk}(\equiv \theta_\kappa)$ is the angle between $\vec{p}_j$ and $\vec{p}_k$ (see Fig. 1).

E. Fitting parameters

After (16) is inserted into expressions (13) and (14), the coefficients of Eq. (11) become

$$|A_{3\pi}|^2 \pm |\overline{A}_{3\pi}|^2$$

$$= \sum_{\kappa\in\{+,-,0\}} |f_\kappa|^2 U_\kappa^\pm$$

$$+ 2 \sum_{\kappa<\sigma\in\{+,-,0\}} (\mathrm{Re}[f_\kappa f_\sigma^*]U_{\kappa\sigma}^{\pm,\mathrm{Re}} - \mathrm{Im}[f_\kappa f_\sigma^*]U_{\kappa\sigma}^{\pm,\mathrm{Im}}),$$

$$(20)$$

$$\mathrm{Im}\left(\frac{q}{p}A_{3\pi}^*\overline{A}_{3\pi}\right)$$

$$= \sum_{\kappa\in\{+,-,0\}} |f_\kappa|^2 I_\kappa$$

$$+ \sum_{\kappa<\sigma\in\{+,-,0\}} (\mathrm{Re}[f_\kappa f_\sigma^*]I_{\kappa\sigma}^{\mathrm{Im}} + \mathrm{Im}[f_\kappa f_\sigma^*]I_{\kappa\sigma}^{\mathrm{Re}}), \qquad (21)$$

with

$$U_\kappa^\pm = |A^\kappa|^2 \pm |\overline{A}^\kappa|^2, \qquad (22)$$

$$I_\kappa = \mathrm{Im}[\overline{A}^\kappa A^{\kappa*}], \qquad (23)$$

$$U_{\kappa\sigma}^{\pm,\mathrm{Re(Im)}} = \mathrm{Re(Im)}[A^\kappa A^{\sigma*} \pm \overline{A}^\kappa \overline{A}^{\sigma*}], \qquad (24)$$

$$I_{\kappa\sigma}^{\mathrm{Re(Im)}} = \mathrm{Re(Im)}[\overline{A}^\kappa A^{\sigma*} - (+)\overline{A}^\sigma A^{\kappa*}]. \qquad (25)$$

The 27 coefficients (22)–(25) are the parameters determined by the fit [22]. The parameters (22)–(25) are called noninterfering and interfering parameters, respectively. This parametrization allows us to describe the differential decay width as a linear combination of independent functions, whose coefficients are the fit parameters in a well-behaved fit. We fix the overall normalization by requiring $U_+^+ = 1$. Thus, 26 of the 27 coefficients are free parameters in the fit.
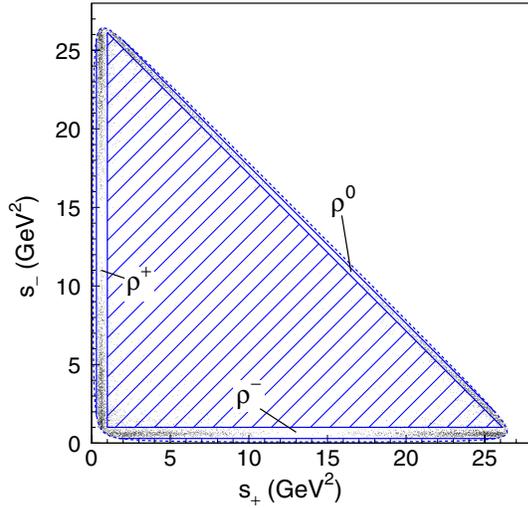
FIG. 2 (color online). Distribution of signal Monte Carlo simulation (without detector efficiency and smearing) in the usual Dalitz plot. The dashed line is the kinematic boundary, while the hatched region corresponds to the region rejected by the mass cut described in Sec. II.

F. Square Dalitz plot (SDP)

The signal and the continuum background $e^+ e^- \to q\bar{q}(q = u, d, s, c)$, which is the dominant background in this analysis, populate the kinematic boundaries of the usual Dalitz plot as shown in Figs. 2 and 3 (left). Since we model part of the Dalitz plot probability density function (PDF) with a binned histogram, the part of the distribution that is concentrated in a narrow region near the edge of the usual Dalitz plot is not easy to treat. We therefore apply the transformation

$$ds_+ ds_- \to |\det J| dm' d\theta', \qquad (26)$$

which defines the SDP [11]. The new coordinates are

$$m' \equiv \frac{1}{\pi} \arccos\left(2\frac{m_0 - m_0^{\min}}{m_0^{\max} - m_0^{\min}} - 1\right), \qquad (27)$$
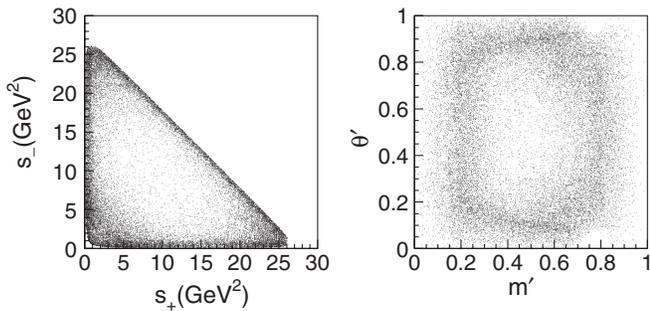
FIG. 3. Distribution of $q\bar{q}$ background (from the data $M_{\rm bc}$ sideband) in the usual Dalitz plot (left panel) and square Dalitz plot (right panel).
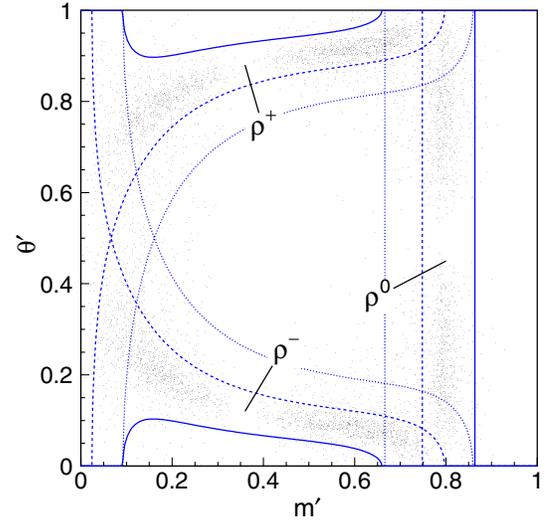
FIG. 4 (color online). Distribution of signal Monte Carlo simulation (without detector efficiency and smearing) in the square Dalitz plot. The solid, dashed, and dotted lines correspond to the isocontours of $\sqrt{s_\kappa} = 0.5$ GeV, 1.0 GeV, and 1.5 GeV, respectively, for each ρ^κ resonance.

$$\theta' \equiv \frac{1}{\pi}\theta_0 \qquad \left(= \frac{1}{\pi}\theta^{-0}\right), \qquad (28)$$

where $m_0 = \sqrt{s_0}$, $m_0^{\max} = m_{B^0} - m_{\pi^0}$, and $m_0^{\min} = 2m_{\pi^+}$ are the kinematic limits of m_0, and J is the Jacobian of the transformation. The determinant of the Jacobian is given by

$$|\det J| = 4|\vec{p}_+||\vec{p}_0|m_0 \cdot \frac{m_0^{\max} - m_0^{\min}}{2} \pi \sin(\pi m')$$
$$\cdot \pi \sin(\pi \theta'), \qquad (29)$$

where $\vec{p}_+$ and $\vec{p}_0$ are the three-momenta of π^+ and π^0 in the $\pi^+ \pi^-$ rest frame. Figures 4 and 3 (right) show the distributions of the signal and continuum events, respectively, in the square Dalitz plot.

II. EVENT SELECTION AND RECONSTRUCTION

To reconstruct candidate $B^0 \to \pi^+ \pi^- \pi^0$ decays, charged tracks reconstructed with the CDC and SVD are required to originate from the interaction point (IP) and to have transverse momenta greater than 0.1 GeV/c. Using kaon identification (KID) information, we distinguish charged kaons from pions based on a kaon (pion) likelihood $\mathcal{L}_{K(\pi)}$ derived from the TOF, ACC, and dE/dx measurements in the CDC. Tracks that are positively identified as electrons are rejected.

Photons are identified as isolated ECL clusters that are not matched to any charged track. We reconstruct π^0 candidates from pairs of photons detected in the barrel (end-cap) ECL with $E_\gamma > 0.05$ (0.1) GeV, where E_γ is the photon energy measured with the ECL. Photon pairs with momenta greater than 0.1 GeV/c in the laboratory

frame and with an invariant mass between 0.1178 GeV/c^2 and 0.1502 GeV/c^2, roughly corresponding to $\pm 3\sigma$ in the mass resolution, are used as π^0 candidates.

We identify B meson decays using the energy difference $\Delta E \equiv E_B^{\text{cms}} - E_{\text{beam}}^{\text{cms}}$ and the beam-energy-constrained mass $M_{\text{bc}} \equiv \sqrt{(E_{\text{beam}}^{\text{cms}})^2 - (p_B^{\text{cms}})^2}$, where $E_{\text{beam}}^{\text{cms}}$ is the beam energy in the cms, and E_B^{cms} and p_B^{cms} are the cms energy and momentum, respectively, of the reconstructed B candidate.

We select candidates in a fit region defined as -0.2 GeV $< \Delta E < 0.2$ GeV and 5.2 GeV/$c^2 < M_{\text{bc}} <$ 5.3 GeV/c^2. The fit region consists of a signal region defined as -0.1 GeV $< \Delta E < 0.08$ GeV and $M_{\text{bc}} >$ 5.27 GeV/c^2, and its complement, called the sideband region, which is dominated by background events.

The vertex position for the $B^0 \to \pi^+ \pi^- \pi^0$ decay is reconstructed using charged tracks that have enough SVD hits [23]. The f_{tag} vertex is obtained with well-reconstructed tracks that are not assigned to f_{CP}. A constraint on the interaction-region profile in the plane perpendicular to the beam axis is also used with the selected tracks.

The b flavor of the accompanying B meson is identified from inclusive properties of particles that are not associated with the reconstructed $B^0 \to f_{CP}$ decay. We use two parameters, the b-flavor charge q_{tag} and r, to represent the tagging information [24]. The parameter r is an event-by-event, Monte Carlo (MC)-determined, flavor-tagging dilution factor that ranges from $r = 0$ for no flavor discrimination to $r = 1$ for unambiguous flavor assignment. It is used only to sort data into six r intervals. The wrong-tag fractions for the six r intervals, w_l ($l = 1, 2, \cdots, 6$), and the differences between B^0 and $\overline{B}^0$ decays, Δw_l, are determined using a high-statistics control sample of semileptonic and hadronic $b \to c$ decays [24–26].

The dominant background for the $B^0 \to \pi^+ \pi^- \pi^0$ signal is from continuum. To distinguish these jetlike events from the spherical B signal events, we combine a set of variables that characterize the event topology into a signal (background) likelihood variable $\mathcal{L}_{\text{sig(bkg)}}$, and impose requirements on the likelihood ratio $\mathcal{R} \equiv \mathcal{L}_{\text{sig}}/(\mathcal{L}_{\text{sig}} + \mathcal{L}_{\text{bkg}})$. Because of a correlation between $\mathcal{R}$ and r, these requirements depend on the quality of flavor tagging.

When more than one candidate in the same event is found in the fit region, we select the best candidate based on the reconstructed π^0 mass and $\mathcal{R}$. About 30% of the signal events have multiple candidates.

After the best candidate selection, we reconstruct the Dalitz variables s_+, s_0, and s_- from (i) the four-momenta of the π^+ and π^-, (ii) the helicity angle of the ρ^0 (i.e., the helicity angle of the $\pi^+ \pi^-$ system), and (iii) the relation of Eq. (2). Note that the energy of the π^0 is not explicitly used here, which improves the resolution of the Dalitz plot variables. We reject candidates that are located in one of the following regions in the Dalitz plot: $\sqrt{s_0} >$

0.95 GeV/c^2 and $\sqrt{s_+} > 1.0$ GeV/c^2 and $\sqrt{s_-} >$ 1.0 GeV/c^2; $\sqrt{s_0} < 0.55$ GeV/c^2 or $\sqrt{s_+} < 0.55$ GeV/c^2 or $\sqrt{s_-} < 0.55$ GeV/c^2 (see Fig. 2). In these regions, the fraction of $B^0 \to \rho\pi$ signal is small. Moreover, radial excitations [the $\rho(1450)$ and $\rho(1700)$] are the dominant contributions to $B^0 \to \pi^+ \pi^- \pi^0$ in the region with $\sqrt{s} >$ 1.0 GeV/c^2, where s is either s_+, s_-, or s_0. Since the amplitudes of the radial excitations are, in general, independent of the amplitude of the $\rho(770)$, they are considered to be background in our analysis; vetoing the high mass region considerably reduces the systematic uncertainties due to their contributions.

Figure 5 shows the M_{bc} and ΔE distributions for the reconstructed $B^0 \to \pi^+ \pi^- \pi^0$ candidates within the ΔE and M_{bc} signal regions, respectively. The signal yield is determined from an unbinned four-dimensional extended-maximum-likelihood fit to the ΔE-M_{bc} and Dalitz plot distribution in the fit region defined above; the Dalitz plot distribution is only used for the events inside the ΔE-M_{bc} signal region. The ΔE-M_{bc} distribution of signal is modeled with binned histograms obtained from MC simulation, where the correlation between ΔE and M_{bc}, the dependence on p_{π^0}, and the difference between data and MC simulation are taken into account. We also take into account incorrectly reconstructed signal events, which we call self-cross-feed (SCF). This component constitutes $\sim 20\%$ of the signal. In a SCF event, either one of the three pions in f_{CP} is swapped with a pion in f_{tag}, or else the π^0 in f_{CP} is misreconstructed. We give the details of the ΔE-M_{bc} and Dalitz plot PDF's of the SCF component in Appendix A. For continuum, we use the ARGUS parametrization [27] for M_{bc} and a linear function for ΔE. The ΔE-M_{bc} distribution of $B\overline{B}$ background is modeled by binned histograms based on MC simulation. The Dalitz plot distributions for all components are modeled in the same way as the time-dependent fit described later, but integrated over the proper time difference, Δt, and summed over the flavor of the tag-side B, q_{tag}. The fit yields 971 ± 42 $B^0 \to \pi^+ \pi^- \pi^0$ events in the signal region, where the error is statistical only.
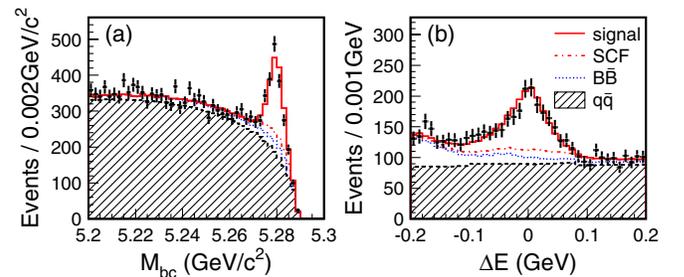
FIG. 5 (color online). The M_{bc} (a) and ΔE (b) distributions within the ΔE and M_{bc} signal regions. The histograms are cumulative. Solid, dot-dashed, dotted, and dashed hatched histograms correspond to correctly reconstructed signal, SCF, $B\overline{B}$, and continuum PDFs, respectively.

III. DETERMINATION OF THE CONTRIBUTIONS FROM RADIAL EXCITATIONS

Although the contributions from radial excitations are suppressed by the selections in the Dalitz plot described in the previous section, there are still significant contributions from the long tails of the radial excitations and their interferences. We thus need to determine the sizes of the radial excitations and their uncertainties to properly model the signal PDF's and systematic uncertainties associated with their degrees of freedom.

Using the same data sample as described above but performing a time-integrated Dalitz plot fit with a wider Dalitz plot acceptance, $0.55 \text{ GeV}/c^2 < \sqrt{s_0} < 1.5 \text{ GeV}/c^2$ or $\sqrt{s_+} < 1.5 \text{ GeV}/c^2$ or $\sqrt{s_-} < 1.5 \text{ GeV}/c^2$, we determine the ρ line shape, i.e., the phases and amplitudes of the coefficients β and γ in Eq. (17). We use these for all of the decay amplitudes. In this fit, we use the PDG values [28] for the masses and widths of the $\rho(1450)$ and $\rho(1700)$. The fit yields

$$|\beta| = 0.31^{+0.07}_{-0.06}, \qquad \arg\beta = (219^{+16}_{-18})^\circ,$$
$$|\gamma| = 0.08^{+0.04}_{-0.03}, \qquad \arg\gamma = (102^{+26}_{-32})^\circ. \qquad (30)$$

The mass distributions and fit results are shown in Fig. 6. Figure 7 schematically shows how the radial excitations contribute to our fit result. Note that the above values are quantities used for the time-dependent Dalitz fit, and we do not regard them as our measurements of β and γ. This is because these parameters are determined from the region where $\rho^+\pi^-$ and $\rho^-\pi^+$ modes, etc., interfere, and they depend on the unfounded common line-shape assumption of Eq. (16); hence we do not give their systematic errors. Because statistics are low, we cannot determine β and γ for each decay mode without imposing the common line-shape assumption. However, we include the effect of possible decay-mode–dependent differences in the values of β and γ in the systematic errors, which are described in Sec. VI A.

FIG. 7 (color online). A schematic figure of the fit result of the line shape and the contributions from radial excitations. Note that our definition of $F_\pi(s)$ does not include the factor $1/(1 + \beta + \gamma)$ as in Eq. (17). The inset shows the high mass region, $m_{\pi\pi} > 1.15 \text{ GeV}/c^2$, on a semilog scale where the interference between the $\rho(770)$ and radial excitations is visible. One can see that the $\rho(770)$ and $\rho(1450)$ destructively interfere with each other near $\sqrt{s} \equiv m_{\pi\pi} = 1.4 \text{ GeV}/c^2$, which means that the $\rho(1450)$ has a large impact on the phase of $F_\pi(s)$, although the absolute value of $|F_\pi(s)|$ is not much affected.

Thus, it is important to determine the common or *average* line shape as well as to obtain an upper limit on the deviation from the average line shape for each of the six decay amplitudes. For this purpose, we put constraints on additional amplitudes that describe (i) the excess in the high mass region, $\sqrt{s} > 0.9 \text{ GeV}/c^2$, where s is either s_+, s_-, or s_0; and (ii) interferences between radial excitations and the lowest resonance $\rho(770)$ [e.g., interferences between $\rho(770)^+\pi^-$ and $\rho(1450)^-\pi^+$, etc.]. The nominal fit is performed with the average line shape determined above, fixing all of the additional amplitudes to zero. When floating the additional amplitudes for the other resonances, we obtain results consistent with zero for all of the additional amplitudes but with large uncertainties compared to the errors for the average line-shape parame-

FIG. 6 (color online). Mass distributions and fitted line shapes in $\rho^+\pi^-$ (left panel), $\rho^-\pi^+$ (middle panel), and $\rho^0\pi^0$ (right panel) enhanced regions. The histograms are cumulative. Solid, dot-dashed, dotted, and dashed hatched histograms correspond to correctly reconstructed signal, SCF, $B\bar{B}$, and continuum PDFs, respectively. Note that there are feed-downs from other quasi-two-body components than those of interest, especially in the high mass regions. For example, the high mass region ($m_0 \gtrsim 1.0 \text{ GeV}/c^2$) of the $\rho^0\pi^0$ enhanced region (right panel) includes large contributions from $\rho^\pm\pi^+$.

ters above. The fit result with the additional line-shape parameters is used in the systematic error study; the uncertainties in these additional line-shape parameters are also taken into account.

IV. TIME-DEPENDENT DALITZ PLOT ANALYSIS

To determine the 26 Dalitz plot parameters, we define the following event-by-event PDF:

$$P(\vec{x}) \equiv f_{\text{sig}}\mathcal{P}_{\text{sig}}(\vec{x}) + f_{B\bar{B}}\mathcal{P}_{B\bar{B}}(\vec{x}) + f_{q\bar{q}}\mathcal{P}_{q\bar{q}}(\vec{x}), \quad (31)$$

where $\mathcal{P}_{\text{sig}}$, $\mathcal{P}_{B\bar{B}}$, and $\mathcal{P}_{q\bar{q}}$ are PDF's for signal, $B\bar{B}$ background, and continuum background, respectively, and f_{sig}, $f_{B\bar{B}}$, and $f_{q\bar{q}}$ are the corresponding fractions that satisfy

$$f_{\text{sig}} + f_{B\bar{B}} + f_{q\bar{q}} = 1. \quad (32)$$

The vector $\vec{x}$, the arguments of the PDF's, corresponds to a set of event-by-event variables:

$$\vec{x} \equiv (\Delta E, M_{\text{bc}}; m', \theta'; \Delta t, q_{\text{tag}}, l; p_{\pi^0}). \quad (33)$$

A detailed description of the PDF can be found in Appendix A.

With the PDF defined above, we form the likelihood function

$$\mathcal{L} \equiv \prod_i P(\vec{x}_i), \quad (34)$$

where i is an index over events. We maximize $\mathcal{L}$ to determine the 26 Dalitz plot parameters using the likelihood function with the signal fraction and the line-shape parameters obtained in Secs. II and III, respectively.

V. FIT RESULT

An unbinned maximum likelihood fit to the 2824 events in the signal region yields the result listed in Table I. The correlation matrix for the 26 parameters, after combining statistical and systematic errors, is shown in Appendix B. Figure 8 shows the projections of the square Dalitz plot in data with the fit result superimposed. We also show the mass and helicity distribution for each $\rho\pi$ enhanced region along with projections of the fit (Fig. 9). We find that U_0^+ is 4.8σ above zero, corresponding to clear evidence for the presence of the decay $B^0 \to \rho^0\pi^0$ in agreement with our previous measurement [29] (see Sec. VIII). Figure 10 shows the Δt distributions and background-subtracted asymmetries. We define the asymmetry in each Δt bin by $(N_+ - N_-)/(N_+ + N_-)$, where $N_{+(-)}$ corresponds to the background-subtracted number of events with $q_{\text{tag}} = +1(-1)$. The $\rho^-\pi^+$ enhanced region shows a significant cosinelike asymmetry, arising from a nonzero value of U_-^-. Note that this is not a *CP*-violating effect, since $\rho^-\pi^+$ is not a *CP* eigenstate. No sinelike asymmetry is observed in any of the $\rho^+\pi^-$, $\rho^-\pi^+$, or $\rho^0\pi^0$ enhanced regions.

TABLE I. Results of the time-dependent Dalitz fit.

	Fit result
U_+^+	+1 (fixed)
U_-^+	$+1.27 \pm 0.13(\text{stat}) \pm 0.09(\text{syst})$
U_0^+	$+0.29 \pm 0.05(\text{stat}) \pm 0.04(\text{syst})$
$U_{+-}^{+,\text{Re}}$	$+0.49 \pm 0.86(\text{stat}) \pm 0.52(\text{syst})$
$U_{+0}^{+,\text{Re}}$	$+0.29 \pm 0.50(\text{stat}) \pm 0.35(\text{syst})$
$U_{-0}^{+,\text{Re}}$	$+0.25 \pm 0.60(\text{stat}) \pm 0.33(\text{syst})$
$U_{+-}^{+,\text{Im}}$	$+1.18 \pm 0.86(\text{stat}) \pm 0.34(\text{syst})$
$U_{+0}^{+,\text{Im}}$	$-0.57 \pm 0.35(\text{stat}) \pm 0.51(\text{syst})$
$U_{-0}^{+,\text{Im}}$	$-1.34 \pm 0.60(\text{stat}) \pm 0.47(\text{syst})$
U_+^-	$+0.23 \pm 0.15(\text{stat}) \pm 0.07(\text{syst})$
U_-^-	$-0.62 \pm 0.16(\text{stat}) \pm 0.08(\text{syst})$
U_0^-	$+0.15 \pm 0.11(\text{stat}) \pm 0.08(\text{syst})$
$U_{+-}^{-,\text{Re}}$	$-1.18 \pm 1.61(\text{stat}) \pm 0.72(\text{syst})$
$U_{+0}^{-,\text{Re}}$	$-2.37 \pm 1.36(\text{stat}) \pm 0.60(\text{syst})$
$U_{-0}^{-,\text{Re}}$	$-0.53 \pm 1.44(\text{stat}) \pm 0.65(\text{syst})$
$U_{+-}^{-,\text{Im}}$	$-2.32 \pm 1.74(\text{stat}) \pm 0.91(\text{syst})$
$U_{+0}^{-,\text{Im}}$	$-0.41 \pm 1.00(\text{stat}) \pm 0.47(\text{syst})$
$U_{-0}^{-,\text{Im}}$	$-0.02 \pm 1.31(\text{stat}) \pm 0.83(\text{syst})$
I_+	$-0.01 \pm 0.11(\text{stat}) \pm 0.04(\text{syst})$
I_-	$+0.09 \pm 0.10(\text{stat}) \pm 0.04(\text{syst})$
I_0	$+0.02 \pm 0.09(\text{stat}) \pm 0.05(\text{syst})$
I_{+-}^{Re}	$+1.21 \pm 2.59(\text{stat}) \pm 0.98(\text{syst})$
I_{+0}^{Re}	$+1.15 \pm 2.26(\text{stat}) \pm 0.92(\text{syst})$
I_{-0}^{Re}	$-0.92 \pm 1.34(\text{stat}) \pm 0.80(\text{syst})$
I_{+-}^{Im}	$-1.93 \pm 2.39(\text{stat}) \pm 0.89(\text{syst})$
I_{+0}^{Im}	$-0.40 \pm 1.86(\text{stat}) \pm 0.85(\text{syst})$
I_{-0}^{Im}	$-2.03 \pm 1.62(\text{stat}) \pm 0.81(\text{syst})$

As a check of our fit, we perform the time-dependent Dalitz plot fit with the B^0 lifetime floated as a free parameter. We obtain 1.41 ± 0.07 ps for the lifetime, where the error is statistical only, while the changes of the other parameters are very small compared to their statistical errors. The lifetime we obtain is consistent with world average [28] and thus validates our understanding of the PDF's and the background fraction.
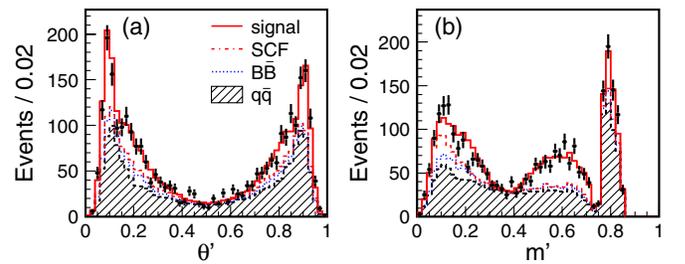
FIG. 8 (color online).   Distributions of θ' (a) and m' (b) with fit results. The histograms are cumulative. Solid, dot-dashed, dotted, and dashed hatched histograms correspond to correctly reconstructed signal, SCF, $B\bar{B}$, and continuum PDFs, respectively.
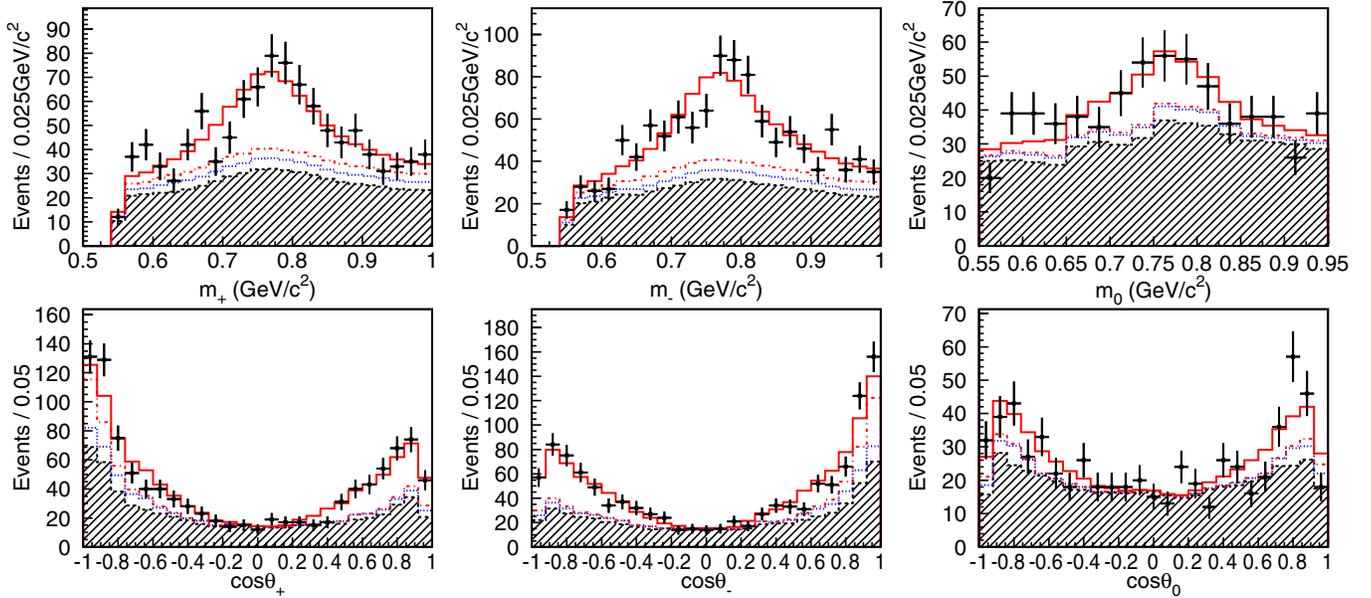
FIG. 9 (color online).   Mass (upper panels) and helicity (lower panels) distribution of $\rho^+\pi^-$ (left panels), $\rho^-\pi^+$ (middle panels), and $\rho^0\pi^0$ (right panels) enhanced regions. The histograms are cumulative. Solid, dot-dashed, dotted, and dashed hatched histograms correspond to correctly reconstructed signal, SCF, $B\bar{B}$, and continuum PDFs, respectively.

Treatment of statistical errors

With a toy MC study, we check the pull distributions, where the pull is defined as the residual divided by the MINOS error. Here, the MINOS error, which corresponds to the deviation from the best fit parameter when $-2\ln(\mathcal{L}/\mathcal{L}_{\max})$ increases by 1, is an estimate of the statistical error. Although the pull is expected to follow a Gaussian distribution with unit width, we find that the width of the pull distribution tends to be significantly larger than 1 for the interfering parameters due to small statistics.
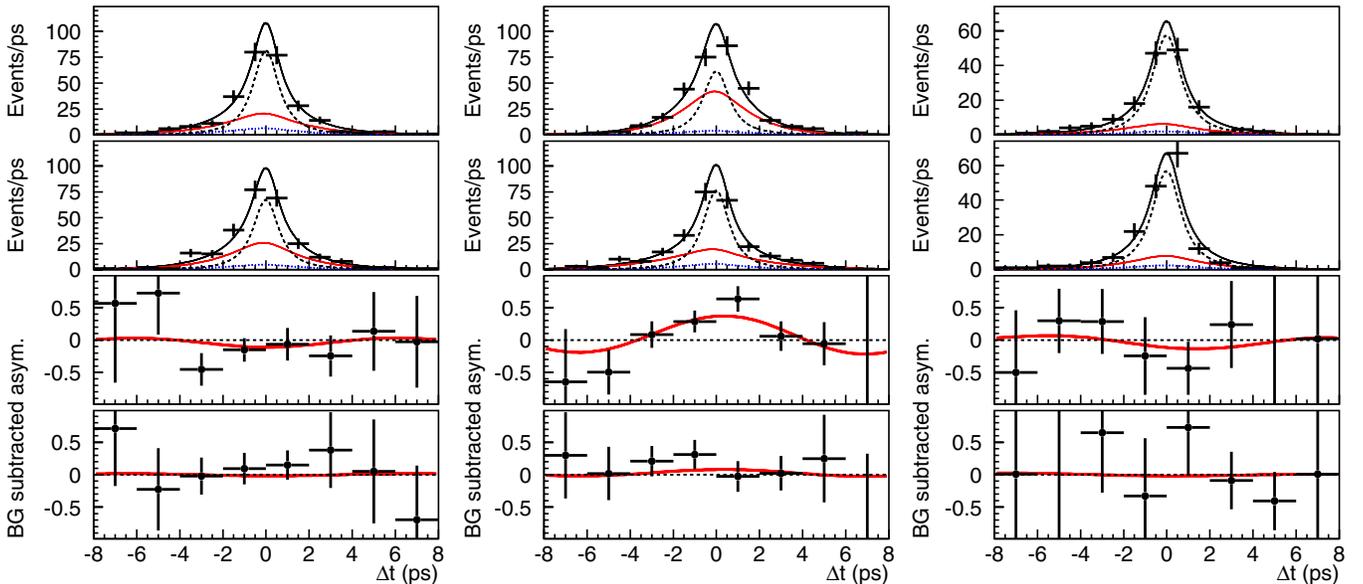
FIG. 10 (color online).   Proper time distributions of good-tag ($r > 0.5$) regions for $f_{\text{tag}} = B^0$ (upper plots) and $f_{\text{tag}} = \overline{B}^0$ (middle upper plots), in $\rho^+\pi^-$ (left plots), $\rho^-\pi^+$ (middle plots), $\rho^0\pi^0$ (right plots) enhanced regions, where solid (red), dotted, and dashed curves correspond to signal, continuum, and $B\bar{B}$ PDFs. The middle lower and lower plots show the background-subtracted asymmetries in the good-tag ($r > 0.5$) and poor-tag ($r < 0.5$) regions, respectively. The significant asymmetry in the $\rho^-\pi^+$ enhanced region (middle plots) corresponds to a nonzero value of U_-^-.

We verify with MC simulation that with high statistics the widths of the pull distributions are unity. To restore the pull width to unity, we multiply the MINOS errors of the interfering parameters by a factor of 1.17, which is the average pull width for the interfering parameters obtained above, and quote the results as the statistical errors. For the noninterfering terms, we quote the MINOS errors without any correction factor.

VI. SYSTEMATIC UNCERTAINTIES

Tables II, III, and IV list the systematic errors for the 26 time-dependent Dalitz plot parameters. The total systematic error is obtained by adding each source of systematic uncertainty in quadrature.

A. Radial excitations (ρ' and ρ'')

The largest contribution for the interfering parameters tends to come from radial excitations. The systematic error related to the radial excitations [$\rho(1450)$ and $\rho(1700)$, or ρ' and ρ''] can be categorized into three classes: (i) uncertainties from the line-shape variation, i.e., the line-shape difference between each decay amplitude, (ii) uncertainties in external parameters, $m_{\rho(1450)}$, $\Gamma_{\rho(1450)}$, $m_{\rho(1700)}$, $\Gamma_{\rho(1700)}$, and (iii) uncertainties in the common line-shape parameters β and γ used for the nominal fit.

In our nominal fit, we assume all six decay amplitudes have the same contribution from $\rho(1450)$ and $\rho(1700)$; i.e., we assume Eq. (16). This assumption, however, is not well grounded. In general, the contributions from $\rho(1450)$ and

TABLE II. Table of systematic errors (1). The notation "<0.01" means that the value is small and less than 0.01, and thus not visible for the number of significant digits shown here. We calculate the total systematic error including these small contributions.

	U_-^+	U_0^+	$U_{+-}^{+,\mathrm{Re}}$	$U_{+0}^{+,\mathrm{Re}}$	$U_{-0}^{+,\mathrm{Re}}$	$U_{+-}^{+,\mathrm{Im}}$	$U_{+0}^{+,\mathrm{Im}}$	$U_{-0}^{+,\mathrm{Im}}$
ρ' and ρ''	0.01	0.01	0.31	0.19	0.19	0.21	0.39	0.30
SCF	0.01	0.02	0.31	0.09	0.11	0.11	0.12	0.11
Signal Dalitz	0.06	0.01	0.15	0.20	0.18	0.13	0.10	0.10
Background Dalitz	0.02	0.01	0.17	0.11	0.11	0.14	0.10	0.19
Other $\pi\pi\pi$	0.04	0.02	0.06	0.08	0.07	0.10	0.09	0.07
Background fraction	0.02	0.01	0.08	0.04	0.07	0.06	0.03	0.11
Physics	0.02	<0.01	0.01	0.01	0.02	0.01	0.01	0.01
Background Δt	<0.01	<0.01	0.03	0.01	0.01	0.02	0.01	0.01
Vertexing	0.03	0.01	0.03	0.05	0.02	0.09	0.05	0.07
Resolution	<0.01	<0.01	0.03	0.05	0.02	0.02	0.02	0.03
Flavor tagging	<0.01	<0.01	<0.01	<0.01	<0.01	<0.01	<0.01	0.01
Fit bias	0.02	0.02	0.10	0.11	0.07	0.06	0.24	0.22
TSI	<0.01	<0.01	0.01	0.02	0.02	0.02	0.01	<0.01
Total	0.09	0.04	0.52	0.35	0.33	0.34	0.51	0.47

TABLE III. Table of systematic errors (2). The notation "<0.01" means that the value is small and less than 0.01, and thus not visible for the number of significant digits shown here. We calculate the total systematic error including these small contributions.

	U_+^-	U_-^-	U_0^-	$U_{+-}^{-,\mathrm{Re}}$	$U_{+0}^{-,\mathrm{Re}}$	$U_{-0}^{-,\mathrm{Re}}$	$U_{+-}^{-,\mathrm{Im}}$	$U_{+0}^{-,\mathrm{Im}}$	$U_{-0}^{-,\mathrm{Im}}$
ρ' and ρ''	0.01	0.02	0.04	0.53	0.29	0.42	0.70	0.31	0.59
SCF	0.02	0.02	0.02	0.09	0.17	0.17	0.13	0.09	0.18
Signal Dalitz	0.01	0.02	0.01	0.27	0.20	0.14	0.30	0.15	0.19
Background Dalitz	0.04	0.03	0.02	0.28	0.32	0.22	0.30	0.20	0.30
Other $\pi\pi\pi$	0.03	0.03	0.02	0.07	0.08	0.12	0.13	0.08	0.08
Background fraction	0.02	0.04	0.01	0.18	0.17	0.14	0.22	0.13	0.11
Physics	0.01	0.01	<0.01	0.03	0.03	0.03	0.04	0.01	0.04
Background Δt	<0.01	<0.01	<0.01	0.02	0.03	0.02	0.03	0.02	0.03
Vertexing	0.02	0.01	0.05	0.18	0.20	0.17	0.08	0.07	0.11
Resolution	0.01	0.01	<0.01	0.10	0.14	0.28	0.07	0.11	0.26
Flavor tagging	0.01	0.01	<0.01	0.03	0.03	0.03	0.05	0.03	0.02
Fit bias	<0.01	0.02	<0.01	0.03	0.09	0.02	0.27	0.08	0.26
TSI	0.03	0.03	0.01	0.06	0.03	0.01	0.05	0.04	0.02
Total	0.07	0.08	0.08	0.72	0.60	0.65	0.91	0.47	0.83

TABLE IV.　Table of systematic errors (3). The notation "<0.01" means that the value is small and less than 0.01, and thus not visible for the number of significant digits shown here. We calculate the total systematic error including these small contributions.

	I_+	I_-	I_0	I_{+-}^{Re}	I_{+0}^{Re}	I_{-0}^{Re}	I_{+-}^{Im}	I_{+0}^{Im}	I_{-0}^{Im}
ρ' and ρ''	0.02	0.02	0.03	0.82	0.64	0.55	0.46	0.56	0.48
SCF	0.01	0.01	0.01	0.18	0.27	0.10	0.38	0.17	0.14
Signal Dalitz	0.01	0.01	0.01	0.28	0.22	0.14	0.27	0.21	0.30
Background Dalitz	0.01	0.01	0.01	0.29	0.35	0.26	0.28	0.26	0.34
Other $\pi\pi\pi$	0.02	0.03	0.01	0.13	0.10	0.10	0.10	0.13	0.14
Background fraction	0.01	0.01	0.01	0.13	0.24	0.19	0.16	0.15	0.25
Physics	0.01	0.01	<0.01	0.04	0.05	0.03	0.04	0.03	0.05
Background Δt	<0.01	<0.01	<0.01	0.05	0.04	0.03	0.05	0.04	0.09
Vertexing	0.02	0.01	0.03	0.11	0.24	0.09	0.31	0.36	0.16
Resolution	0.01	0.01	0.01	0.19	0.22	0.15	0.28	0.20	0.23
Flavor tagging	<0.01	<0.01	<0.01	0.04	0.07	0.04	0.04	0.07	0.03
Fit bias	<0.01	0.01	<0.01	0.11	0.10	0.41	0.25	0.13	0.18
TSI	<0.01	<0.01	<0.01	0.09	0.04	0.06	0.05	0.18	0.05
Total	0.04	0.04	0.05	0.98	0.92	0.80	0.89	0.85	0.81

$\rho(1700)$ can be different for each of the decay amplitudes, and thus the systematic uncertainty from this assumption must be addressed. Without the assumption about the higher resonances, Eq. (16) becomes

$$\overset{(-)}{f}_\kappa = T_1^\kappa \overset{(-)}{F}{}_\pi^\kappa(s_\kappa), \qquad (35)$$

where

$$\overset{(-)}{F}{}_\pi^\kappa(s) \equiv \mathrm{BW}_{\rho(770)}(s) + (\beta + \Delta\overset{(-)}{\beta}_\kappa)\mathrm{BW}_{\rho(1450)}(s)$$

$$+ (\gamma + \Delta\overset{(-)}{\gamma}_\kappa)\mathrm{BW}_{\rho(1700)}(s). \qquad (36)$$

The variation of the contributions from radial excitations is described by nonzero $\Delta\overset{(-)}{\beta}_\kappa$ and $\Delta\overset{(-)}{\gamma}_\kappa$, which are 12 complex variables. We generate various toy MC-simulated samples, where the inputs A^κ and $\overline{A}^\kappa$ are fixed but the values of $\Delta\overset{(-)}{\beta}_\kappa$ and $\Delta\overset{(-)}{\gamma}_\kappa$ are varied randomly within the constraints on $\Delta\overset{(-)}{\beta}_\kappa$ and $\Delta\overset{(-)}{\gamma}_\kappa$; these constraints are obtained from the results in Sec. III, which are combined with the isospin relation [7,8] to improve the constraints. The statistics for each pseudoexperiment are set to be large enough so that the statistical uncertainty is negligible. We assign the changes in the fit results as well as the MC biases due to the changes in $\Delta\overset{(-)}{\beta}_\kappa$ and $\Delta\overset{(-)}{\gamma}_\kappa$ as systematic errors.

For the masses and widths of the $\rho(1450)$ and $\rho(1700)$, we use the values from the PDG [28]. To estimate the systematic error originating from uncertainties in their parameters, we generate toy MC-simulated samples varying the input masses and widths. We fit them using parametrizations with the masses and widths of the nominal fit. Here, we vary the masses by twice the PDG error [$\pm$ 50 MeV/c^2 for the $\rho(1450)$ and ± 40 MeV/c^2 for the

$\rho(1700)$] since the variations between independent experiments are much larger than the 1σ PDG errors, while we vary the widths by the $\pm 1\sigma$ PDG errors. We quote the mean shift of the toy MC-simulation ensemble as the systematic error. We also take into account the systematic errors from the uncertainties in β and γ for the nominal fit [Eq. (30)] in the same way.

B. SCF

Systematic errors due to SCF are dominated by the uncertainty in the difference between data and MC simulation; these errors are determined from $B \to D^{(*)}\rho$ control samples that contain a single π^0 in the final state. We vary the amount of SCF by its 1σ error, which is $\pm 100\%$ for the CR SCF and $^{+30(60)}_{-30}\%$ for the NR SCF in DS-I (DS-II), where DS-I and DS-II denote the subsets of data taken with the different detector configurations defined in Sec. I A. Here, NR represents the neutral-pion-replaced SCF and CR represents the charged-pion-replaced SCF. We quote the differences from the nominal fit as the systematic error. The event fraction for each r region (for CR and NR), the wrong-tag fractions (for CR), and lifetime used in the Δt PDF (for CR), which are obtained from MC simulation, are also varied, and the differences in the fit results are assigned as a systematic error.

C. Signal Dalitz PDF

Systematic errors due to the Dalitz PDF for signal are mainly from the Dalitz-plot-dependent efficiency. We take account of MC simulation statistics in the efficiency and uncertainty in the π^0 momentum-dependent efficiency correction, $\epsilon'(p_{\pi^0})$, obtained from the control samples of the decay modes $\overline{B}^0 \to \rho^- D^{(*)+}$, $\overline{B}^0 \to \pi^- D^{(*)+}$, $B^- \to \rho^- D^{(*)0}$, and $B^- \to \pi^- D^{(*)0}$. The Dalitz plot efficiency

obtained from MC simulation is found to have a small charge asymmetry ($\sim 3\%$ at most). We use this asymmetric efficiency for our nominal fit. To estimate the systematic error from the asymmetry, we fit the data using a symmetric efficiency and conservatively quote twice the difference between symmetric and asymmetric efficiencies as the systematic error. The Dalitz plot efficiency is *r*-region dependent and obtained as a product with the event fraction in the corresponding region, $\mathcal{F}^l_{\text{sig}} \cdot \epsilon^l(m', \theta')$, using MC simulation. The difference in the fraction for data and MC simulation is estimated to be $\sim 10\%$ using the $B^0 \to D^{*-}\pi^+$ control sample. The fractions are varied by $\pm 10\%$ to estimate the systematic error.

D. Background Dalitz PDF

The Dalitz plot for continuum background has an uncertainty due to the limited statistics of the sideband events, which we use to model the PDF. We estimate the uncertainty by performing a toy MC study of sideband events. With each MC pseudoexperiment, we model the PDF in the same way as we do for real data. Using the PDF, we fit the data in the signal region and quote the variation of fit results as the systematic error. The flavor-asymmetry parameters for the continuum background, which are fitted from sideband events, are varied by their uncertainties. Systematic uncertainty from the statistics of the $B\overline{B}$ MC simulation, which is used to model the $B\overline{B}$ Dalitz plot PDF, is also taken into account.

E. $B^0 \to \pi^+\pi^-\pi^0$ processes other than $B^0 \to (\rho\pi)^0$

The primary contribution to the systematic errors of the noninterfering parameters tends to come from the $B^0 \to \pi^+\pi^-\pi^0$ decay processes that are not $B^0 \to (\rho\pi)^0$. We take account of the contributions from $B^0 \to f_0(980)\pi^0$, $B^0 \to f_0(600)\pi^0$, $B^0 \to \omega\pi^0$, and nonresonant $B^0 \to \pi^+\pi^-\pi^0$. Upper limits on their contributions are determined from data, except for $B^0 \to \omega\pi^0$, for which we use world averages for $\mathcal{B}(B^0 \to \omega\pi^0)$ [30] and $\mathcal{B}(\omega \to \pi^+\pi^-)$ [28]. For the mass and width parameters of the $f_0(600)$ resonance, we use recent measurements by BES [31], CLEO [32], and E791 [33] and take the largest variation. We find no significant signals for any of the above decay modes. Using the 1σ upper limits as input, we generate toy MC simulation for each mode with the interference between the $B^0 \to (\rho\pi)^0$ and the other $B^0 \to \pi^+\pi^-\pi^0$ mode taken into account. We obtain the systematic error by fitting the toy MC simulation assuming $B^0 \to (\rho\pi)^0$ only in the PDF. Within the physically allowed regions, we vary the *CP* violation parameters of the other $B^0 \to \pi^+\pi^-\pi^0$ modes and the relative phase difference between $B^0 \to (\rho\pi)^0$ and the other $B^0 \to \pi^+\pi^-\pi^0$ modes, and use the largest deviation as the systematic error for each decay mode.

In the above procedure, we use relativistic Breit-Wigner functions for the $f_0(980)$ and $f_0(600)$. To validate the estimated systematic uncertainties, we investigate possible model dependence as follows. For the $f_0(980)$, we perform the same procedure using a coupled-channel Breit-Wigner function [34], which takes account of the opening of the $K\overline{K}$ decay channel, instead of a simple relativistic Breit-Wigner function. We observe no systematic increase in the uncertainties. By changing the model for the $f_0(980)$, the total systematic error for the "$\pi^+\pi^-\pi^0$ other than $\rho\pi$" category increases by at most 10% in the noninterfering parameters, which are the only parameters in which the systematic error contribution from this category is significant. Thus, we conclude that the model dependence of the $f_0(980)$ resonance parametrization is negligibly small. For the $f_0(600)$, the situation is more complicated because there are not only possible variations of the resonance mass spectrum but also uncertainties in the low mass $\pi^-\pi^+$ *S*-wave component; this contribution may not be modeled by a simple scalar resonance such as the $f_0(600)$, but by a more sophisticated description known as the *K* matrix [35,36]. To address this issue in a model-independent and conservative way, we perform the systematic error study assuming a hypothetical scalar resonance that has exactly the same mass spectrum as the $\rho^0(770)$. Since this resonance, as a $\pi^+\pi^-$ *S*-wave contribution, is maximally similar to the $\rho^0\pi^0$ signal, this procedure will lead to systematic uncertainties larger than, or at least comparable to, any other model of the $\pi^+\pi^-$ *S*-wave contribution. We find that including the hypothetical resonance leads to no significant increase of the systematic uncertainties compared to those we assigned to the $f_0(600)$ in our nominal systematic errors. The increase compared to the case of the $f_0(600)$ is at most 30% in the noninterfering parameters, which corresponds to only a 10% increase of the total systematic error for the "$\pi^+\pi^-\pi^0$ other than $\rho\pi$" category. This follows because the discrimination power of the $\rho^0\pi^0$ signal from these low-mass $\pi^+\pi^-$ *S*-wave contributions, in general, primarily comes from the helicity distribution; the result is not sensitive to the details of the models of the low mass $\pi^+\pi^-$ distributions. Thus, the systematic uncertainties that we have assigned for a possible contribution from $B^0 \to f_0(600)\pi^0$ are reasonable estimates of the systematic uncertainties from possible $B^0 \to$ (low mass $\pi^+\pi^-$ *S*-wave) π^0 contributions in general.

F. Background fraction

Systematic errors due to the event-by-event ΔE-M_{bc} background fractions are studied by varying the PDF shape parameters; the fraction of continuum background; and a correction factor to the signal PDF shape, which takes account of the difference between data and MC simulation, by $\pm 1\sigma$. We also vary the fractions of the $B\overline{B}$ background, which are estimated with MC simulation, by $\pm 50\%$ ($\pm 20\%$) for $b \to c$ ($b \to u$) processes.

G. Physics parameters

We use world averages [28,30] for the following physics parameters: τ_{B^0} and Δm_d (used for signal and $B\overline{B}$ background Δt), the CKM angles ϕ_1 and ϕ_2 (used in $B\overline{B}$ background), and the branching fractions of $b \to u$ decay modes (used in $B\overline{B}$ background). The systematic error is assigned by varying these parameters by $\pm 1\sigma$. The charge asymmetry of $B^0 \to a_1^\pm \pi^\mp$, for which we use zero in the nominal fit, is varied over the physically allowed region, i.e., ± 1.

H. Background Δt PDF

Systematic errors from uncertainties in the background Δt shapes for both continuum and $B\overline{B}$ backgrounds are estimated by varying each parameter by $\pm 1\sigma$.

I. Vertex reconstruction

To determine the systematic error that arises from uncertainties in the vertex reconstruction, the track and vertex selection criteria are varied to search for possible systematic biases. In addition to the tracks, the IP constraint is also used in the vertex reconstruction with the smearing due to B-flight distance taken into account. The systematic error due to the IP constraint is estimated by varying the smearing by $\pm 10~\mu$m.

J. Resolution function for the Δt PDF

Systematic errors due to uncertainties in the resolution function are estimated by varying each resolution parameter obtained from data (MC simulation) by $\pm 1\sigma$ ($\pm 2\sigma$). Systematic errors due to uncertainties in the wrong-tag fractions are also studied by varying the wrong-tag fraction individually for each r region.

K. Fit bias

We observed fit biases due to small statistics for some of the fitted parameters. Since these biases are much smaller than the statistical errors, we do not correct for them but rather take them into account in the systematic errors. For each parameter, we estimate the size of the fit bias from a toy MC study and quote the bias in the systematic errors. We also confirm that the bias is consistent between toy MC and full detector MC simulation.

L. Tag-side interference

Finally, we investigate the effects of tag-side interference (TSI), which is the interference between CKM-favored and CKM-suppressed $B \to D$ transitions in the f_{tag} final state [37]. A small correction to the PDF for the signal distribution arises from the interference. We estimate the size of the correction using a $B^0 \to D^{*-}\ell^+\nu$ control sample. We then generate MC pseudoexperiments and make an ensemble test to obtain the systematic biases.

VII. QUASI-TWO-BODY PARAMETERS

One can deduce quasi-two-body *CP*-violation parameters from the fit result of the time-dependent Dalitz plot analysis. In this section, we obtain the quasi-two-body *CP*-violation parameters from the results for the U and I parameters determined in the previous section.

The time-dependent partial width for the quasi-two-body decay process of $B^0 \to \rho^\pm\pi^\mp$ is given by [38]

$$\frac{d\Gamma}{d\Delta t} \propto (1 \pm \mathcal{A}_{\rho\pi}^{CP})e^{-|\Delta t|/\tau_{B^0}}$$
$$\times [1 - q_{\text{tag}}(\mathcal{C} \pm \Delta\mathcal{C})\cos(\Delta m_d \Delta t)$$
$$+ q_{\text{tag}}(\mathcal{S} \pm \Delta\mathcal{S})\sin(\Delta m_d \Delta t)], \qquad (37)$$

where the upper (lower) sign is taken for $B^0 \to \rho^+\pi^-$ ($\rho^-\pi^+$). The parameters $\mathcal{A}_{\rho\pi}^{CP}, \mathcal{C}, \Delta\mathcal{C}, \mathcal{S}$, and $\Delta\mathcal{S}$ characterize *CP*-violating and charge-asymmetric properties of $B^0 \to \rho^\pm\pi^\mp$; $\mathcal{A}_{\rho\pi}^{CP}$ is a time- and flavor-integrated charge asymmetry, $\mathcal{C}$ is a flavor-dependent direct *CP*-violation parameter, $\mathcal{S}$ is a mixing-induced *CP*-violation parameter, and $\Delta\mathcal{C}$ and $\Delta\mathcal{S}$ are *CP*-conserving parameters (i.e., nonzero $\Delta\mathcal{C}$ or $\Delta\mathcal{S}$ does not imply *CP* violation). They are related to the parameters obtained in the time-dependent Dalitz plot analysis as

$$\mathcal{A}_{\rho\pi}^{CP} = \frac{U_+^+ - U_-^+}{U_+^+ + U_-^+},$$
$$\mathcal{C} \equiv \frac{\mathcal{C}^+ + \mathcal{C}^-}{2}, \qquad \Delta\mathcal{C} \equiv \frac{\mathcal{C}^+ - \mathcal{C}^-}{2},$$
$$\mathcal{S} \equiv \frac{\mathcal{S}^+ + \mathcal{S}^-}{2}, \qquad \Delta\mathcal{S} \equiv \frac{\mathcal{S}^+ - \mathcal{S}^-}{2}, \qquad (38)$$

where

$$\mathcal{C}^+ = \frac{U_+^-}{U_+^+}, \qquad \mathcal{C}^- = \frac{U_-^-}{U_-^+}, \qquad \mathcal{S}^+ = \frac{2I_+}{U_+^+}, \qquad \mathcal{S}^- = \frac{2I_-}{U_-^+}. \qquad (39)$$

We obtain

$$\mathcal{A}_{\rho\pi}^{CP} = -0.12 \pm 0.05 \pm 0.04, \qquad (40)$$

$$\mathcal{C} = -0.13 \pm 0.09 \pm 0.05, \qquad (41)$$

$$\Delta\mathcal{C} = +0.36 \pm 0.10 \pm 0.05, \qquad (42)$$

$$\mathcal{S} = +0.06 \pm 0.13 \pm 0.05, \qquad (43)$$

$$\Delta\mathcal{S} = -0.08 \pm 0.13 \pm 0.05, \qquad (44)$$

where first and second errors are statistical and systematic, respectively. The correlation matrix is shown in Table V.

The angle ϕ_2^{eff}, which equals ϕ_2 in the no-penguin limit, can be defined as [39]

$$\phi_2^{\text{eff}} \equiv \tfrac{1}{2}(\phi_2^{\text{eff},+} + \phi_2^{\text{eff},-}) \qquad (45)$$

with

TABLE V.   Correlation matrix of the quasi-two-body parameters, with statistical and systematic errors combined.

	$\mathcal{A}_{\rho\pi}^{CP}$	$\mathcal{C}$	$\Delta\mathcal{C}$	$\mathcal{S}$	$\Delta\mathcal{S}$
$\mathcal{A}_{\rho\pi}^{CP}$	+1.00				
$\mathcal{C}$	−0.17	+1.00			
$\Delta\mathcal{C}$	+0.09	+0.16	+1.00		
$\mathcal{S}$	+0.01	−0.02	−0.00	+1.00	
$\Delta\mathcal{S}$	−0.00	−0.01	−0.02	+0.29	+1.00

$$2\phi_2^{\text{eff},\pm} \pm \hat{\delta} = \arcsin\left(\frac{\mathcal{S} \pm \Delta\mathcal{S}}{\sqrt{1 - (\mathcal{C} \pm \Delta\mathcal{C})^2}}\right), \quad (46)$$

and

$$\hat{\delta} = \arg(A^{-*}A^+). \quad (47)$$

Our measurement gives

$$\phi_2^{\text{eff}} = (88.0 \pm 3.9 \pm 1.7)^\circ, \quad (48)$$

where $\phi_2^{\text{eff}} \sim 90^\circ$ would give values of $\mathcal{S}$ and $\Delta\mathcal{S}$ consistent with zero. There also exists a mirror solution $\phi_2^{\text{eff}} = (2.0 \pm 3.9 \pm 1.7)^\circ$ due to the twofold ambiguity in the arcsine. In addition, other solutions, $\phi_2^{\text{eff}} \sim 45^\circ$ and 135°, are also allowed, in principle. The additional solutions correspond to cases where $2\phi_2^{\text{eff},+} + \hat{\delta}$ and $2\phi_2^{\text{eff},-} - \hat{\delta}$ differ by $\sim 180^\circ$; they can be excluded by including a weak theoretical assumption [flavor $SU(3)$ or QCD factorization implies a much smaller value] [39]. The measured ϕ_2^{eff} can be used to constrain ϕ_2 in a model-dependent way, using a theoretical assumption that puts a limit on the difference $\phi_2 - \phi_2^{\text{eff}}$ [39,40].

The direct *CP*-violation parameters for the process $B^0 \rightarrow \rho^\pm\pi^\mp$, $\mathcal{A}_{\rho\pi}^{+-}$ and $\mathcal{A}_{\rho\pi}^{-+}$, are defined as

$$\mathcal{A}_{\rho\pi}^{+-} = \frac{\Gamma(\overline{B}^0 \rightarrow \rho^-\pi^+) - \Gamma(B^0 \rightarrow \rho^+\pi^-)}{\Gamma(\overline{B}^0 \rightarrow \rho^-\pi^+) + \Gamma(B^0 \rightarrow \rho^+\pi^-)} \quad (49)$$

and

$$\mathcal{A}_{\rho\pi}^{-+} = \frac{\Gamma(\overline{B}^0 \rightarrow \rho^+\pi^-) - \Gamma(B^0 \rightarrow \rho^-\pi^+)}{\Gamma(\overline{B}^0 \rightarrow \rho^+\pi^-) + \Gamma(B^0 \rightarrow \rho^-\pi^+)}. \quad (50)$$

One can transform the parameters $\mathcal{A}_{\rho\pi}^{CP}$, $\mathcal{C}$, and $\Delta\mathcal{C}$ into the direct *CP* violation parameters as

$$\mathcal{A}_{\rho\pi}^{+-} = -\frac{\mathcal{A}_{\rho\pi}^{CP} + \mathcal{C} + \mathcal{A}_{\rho\pi}^{CP}\Delta\mathcal{C}}{1 + \Delta\mathcal{C} + \mathcal{A}_{\rho\pi}^{CP}\mathcal{C}}, \quad (51)$$

$$\mathcal{A}_{\rho\pi}^{-+} = \frac{\mathcal{A}_{\rho\pi}^{CP} - \mathcal{C} - \mathcal{A}_{\rho\pi}^{CP}\Delta\mathcal{C}}{1 - \Delta\mathcal{C} - \mathcal{A}_{\rho\pi}^{CP}\mathcal{C}}. \quad (52)$$

We obtain

$$\mathcal{A}_{\rho\pi}^{+-} = +0.21 \pm 0.08 \pm 0.04, \quad (53)$$
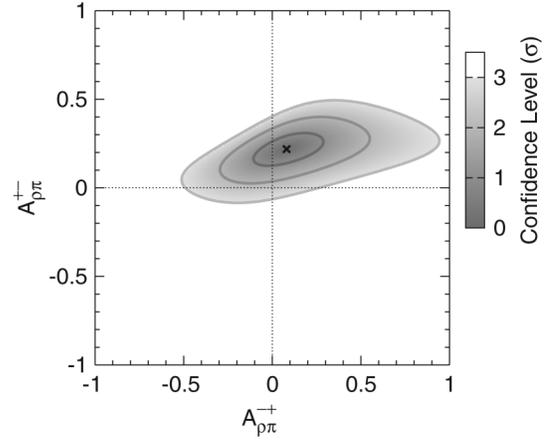
FIG. 11.   Contour plot of the confidence level for the direct *CP* violation parameters $\mathcal{A}_{\rho\pi}^{+-}$ vs $\mathcal{A}_{\rho\pi}^{-+}$.

$$\mathcal{A}_{\rho\pi}^{-+} = +0.08 \pm 0.16 \pm 0.11, \quad (54)$$

with a correlation coefficient of $+0.47$. Our result differs from the case of no direct *CP* asymmetry ($\mathcal{A}_{\rho\pi}^{+-} = 0$ and $\mathcal{A}_{\rho\pi}^{-+} = 0$) by 2.3 standard deviations (Fig. 11).

We also measure the *CP* violating parameters of the quasi-two-body $B^0 \rightarrow \rho^0\pi^0$ decay process. The time-dependent partial width for the process is given as

$$\frac{d\Gamma}{d\Delta t} \propto e^{-|\Delta t|/\tau_{B^0}}[1 + q_{\text{tag}}\mathcal{A}_{\rho^0\pi^0}\cos(\Delta m_d\Delta t)$$
$$+ q_{\text{tag}}\mathcal{S}_{\rho^0\pi^0}\sin(\Delta m_d\Delta t)], \quad (55)$$

where $\mathcal{A}_{\rho^0\pi^0}$ and $\mathcal{S}_{\rho^0\pi^0}$ are the parameters to be measured. They are calculated from the parameters fitted in the time-dependent Dalitz plot analysis as

$$\mathcal{A}_{\rho^0\pi^0} = -\frac{U_0^-}{U_0^+}, \qquad \mathcal{S}_{\rho^0\pi^0} = \frac{2I_0}{U_0^+}. \quad (56)$$

We obtain

$$\mathcal{A}_{\rho^0\pi^0} = -0.49 \pm 0.36 \pm 0.28, \quad (57)$$

$$\mathcal{S}_{\rho^0\pi^0} = +0.17 \pm 0.57 \pm 0.35, \quad (58)$$

with a correlation coefficient of -0.08. We observe a very small correlation between the quasi-two-body *CP*-violation parameters of the processes $B^0 \rightarrow \rho^\pm\pi^\mp$ and $B^0 \rightarrow \rho^0\pi^0$, whose absolute values are less than about 0.02. Our measurement of $\mathcal{A}_{\rho^0\pi^0}$ is consistent with the previous measurement from Belle [29].

VIII. BRANCHING FRACTION MEASUREMENTS

The number of $B^0 \rightarrow \pi^+\pi^-\pi^0$ events, N_{sig}, obtained in Sec. II is

$$N_{\text{sig}} = 971 \pm 42. \quad (59)$$

The branching fraction for $B^0 \rightarrow (\rho\pi)^0 \rightarrow \pi^+\pi^-\pi^0$ including radial excitations is given as

$$\mathcal{B}(B^0 \rightarrow \rho\pi^{\text{all}}) = \frac{N_{\text{sig}}}{N_{B\bar{B}}\epsilon^{\text{Det}}\epsilon^{\text{Veto}}\epsilon'^{\text{KID}}}, \quad (60)$$

where ϵ^{Det} and ϵ^{Veto} are the average detection efficiency and the efficiency corresponding to the Dalitz veto (i.e., the upper and lower bounds on s_+, s_-, and s_0), respectively; ϵ'^{KID} is the efficiency correction factor to take account of the KID difference between data and MC simulation; and $N_{B\bar{B}}$ is the number of $B\bar{B}$ pairs produced, where we assume equal numbers of $B^0\bar{B}^0$ and B^+B^- pairs. The branching fraction for the decay to a ground state $\rho^\kappa(770)\pi^\sigma$ is given as

$$\mathcal{B}(B^0 \rightarrow \rho^\kappa(770)\pi^\sigma) = f_{\rho^\kappa_{\text{all}}}f_{\rho^\kappa(770)}\mathcal{B}(B^0 \rightarrow \rho\pi^{\text{all}})$$

$$([\kappa, \sigma] = [\pm, \mp], [0, 0]), \quad (61)$$

where $f_{\rho^\kappa_{\text{all}}}$ and $f_{\rho^\kappa(770)}$ are the fractions of $B^0 \rightarrow \rho^\kappa_{\text{all}}\pi^\sigma$ among all $B^0 \rightarrow \rho\pi^{\text{all}} \rightarrow \pi^+\pi^-\pi^0$ and that of $B^0 \rightarrow \rho^\kappa(770)\pi^\sigma$ among $B^0 \rightarrow \rho^\kappa_{\text{all}}\pi^\sigma$, respectively. Here, ρ^κ_{all} symbolically represents the total contribution from $\rho^\kappa(770)$, $\rho^\kappa(1450)$, and $\rho^\kappa(1700)$. The fraction $f_{\rho^\kappa_{\text{all}}}$ is calculated from the parameters U^+_κ and $U^{+,\text{Re(Im)}}_{\kappa\sigma}$ ($\kappa, \sigma = +, -, 0$) in Table I, while the coefficients representing contributions from radial excitations (β, γ) in Eq. (30) determine $f_{\rho^\kappa(770)}$. More details of the formalism can be found in Appendix C. The values for these coefficients are shown in Table VI. Note that $f_{\rho^\kappa(770)}$ is close to 1 and $|1 - f_{\rho^\kappa(770)}|$ is much smaller than the error in our result. This means that it is reasonable to compare the central values of our result with the preceding branching fraction measurements that do not separate the contribution from radial excitations. However, the errors are not directly comparable.

From (59) and the coefficients in Table VI, we obtain

$$\mathcal{B}(B^0 \rightarrow \rho\pi^{\text{all}}) = (25.8 \pm 1.2 \pm 3.6) \times 10^{-6}, \quad (62)$$

and

$$\mathcal{B}(B^0 \rightarrow \rho^\pm(770)\pi^\mp) = (22.6 \pm 1.1 \pm 4.4) \times 10^{-6},$$

$$\mathcal{B}(B^0 \rightarrow \rho^0(770)\pi^0) = (3.0 \pm 0.5 \pm 0.7) \times 10^{-6}. \quad (63)$$

TABLE VI. Summary of the coefficients used in the branching fraction measurement.

ϵ^{Det}	0.10
ϵ^{Veto}	0.84
ϵ'^{KID}	0.96
$f_{\rho^\pm_{\text{all}}}$	0.89
$f_{\rho^0_{\text{all}}}$	0.12
$f_{\rho^\pm(770)}$	0.99
$f_{\rho^0(770)}$	0.99

TABLE VII. Summary table of the systematic errors for the branching fraction measurements. A common factor of $\times 10^{-6}$ is omitted for simplicity.

	$\rho\pi^{\text{all}}$	$\rho^\pm(770)\pi^\mp$	$\rho^0(770)\pi^0$
ρ' and ρ''	± 2.8	± 3.9	± 0.5
Physics parameters	± 0.1	± 0.1	± 0.0
Fit	± 1.7	± 1.5	± 0.2
Detection efficiency	± 1.4	± 1.3	± 0.2
TDPA systematic	± 0.2	± 0.4	± 0.4
Number of $B\bar{B}$	± 0.3	± 0.3	± 0.0
Total	± 3.6	± 4.4	± 0.7

Here, the first and second errors correspond to the statistical and systematic errors, respectively, where statistical errors include the contributions from the statistical errors on the number of events (N_{sig}) and uncertainties in the Dalitz parameters $(U^+_\kappa$ and $U^{+,\text{Re(Im)}}_{\kappa\sigma})$. The correlation coefficient for the statistical errors between $\mathcal{B}(B^0 \rightarrow \rho^\pm(770)\pi^\mp)$ and $\mathcal{B}(B^0 \rightarrow \rho^0(770)\pi^0)$ is -0.09. The branching fractions obtained are consistent with our previous measurements [29,41].

A. Systematic uncertainties

Table VII summarizes the systematic errors for the branching fraction measurement. We discuss each item in the table in the following.

1. Radial excitations (ρ' and ρ'')

As in the time-dependent analysis, the systematic uncertainties related to the radial excitations come from (i) uncertainties due to line-shape variation, (ii) uncertainties in masses and widths of the $\rho(770)$ and its radial excitations, and (iii) the common line-shape parameters. Their impacts are estimated in the same manner as done for the time-dependent analysis. The impact from possible line-shape variation, which is constrained by our data, is estimated by a MC study. We adopt the same uncertainties for the masses and widths of the $\rho(770)$ and radial excitations as in the time-dependent analysis and estimate their impact on the branching fractions. The errors due to common line-shape parameters (β, γ) are also taken into account.

The uncertainty for this category is sizable since the $\rho(770)$ and radial excitations are separated in the branching fraction analysis. This is an essential difference from the time-dependent analysis, where we do not separate the $\rho(770)$ and the radial excitations.

2. Physics parameters

This category includes the systematic error from the uncertainties in the branching fractions of the $B\bar{B}$ background components as well as those due to the possible

TABLE VIII. Summary of the systematic uncertainties related to the detection efficiency.

π^0 detection	4.7%
Kaon identification	0.4%
Continuum suppression	2.3%
Vertex reconstruction	1.8%
Dalitz efficiency	0.8%

contribution from the $B^0 \rightarrow \pi^+ \pi^- \pi^0$ processes other than $B^0 \rightarrow (\rho\pi)^0$.

3. Fit

This category includes the uncertainties related to the extended unbinned maximum likelihood fit, except for the items included in the above two categories. It consists of the uncertainties from the modeling of PDF used in the fit, where the possible uncertainty in the SCF component has a sizable impact; the fraction of the $B\overline{B}$ background component, which is fixed in the nominal fit; and the fit bias.

4. Detection efficiency

The largest components of the detection efficiency systematic uncertainty are the differences between data and MC simulation. We consider differences in π^0 detection efficiency with π^0 momentum dependence, the KID efficiency correction (ϵ'^{KID}), the continuum event suppression cut, and the vertex reconstruction efficiency. All are estimated from control sample studies. Small uncertainty due to the limited statistics of MC simulation used in calculation of the efficiency is also taken into account. Table VIII shows the breakdown of the systematic uncertainty contributions from the above items.

5. Time-dependent Dalitz plot analysis (TDPA) systematic errors

The systematic errors in the Dalitz plot parameters obtained in the TDPA listed in Table I propagate to the branching fractions.

6. Number of $B\overline{B}$ pairs

The number of accumulated $B\overline{B}$ pairs and its uncertainty are $N_{B\overline{B}} = (449.3 \pm 5.7) \times 10^6$, assuming an equal production rate for charged and neutral $B\overline{B}$ pairs from the $\Upsilon(4S)$. The uncertainty in the number of $B\overline{B}$ pairs propagates to the branching fraction and is taken into account as a systematic error.

IX. CONSTRAINT ON THE CKM ANGLE ϕ_2

We constrain the CKM angle ϕ_2 from our analysis following the procedure described in Ref. [6]. With three $B^0 \rightarrow (\rho\pi)^0$ decay modes, we have nine free parameters including ϕ_2:

$$9 = (6 \text{ complex amplitudes} = 12 \text{ d.o.f.}) + \phi_2$$
$$- (1 \text{ global phase}) - (1 \text{ global normalization})$$
$$- (1 \text{ isospin relation} = 2 \text{ d.o.f.}), \quad (64)$$

where we make use of an isospin relation that relates neutral B decay processes only [7,8]. Parametrizing the six complex amplitudes with nine free parameters, we form a χ^2 function using the 26 measurements from our time-dependent Dalitz plot analysis as constraints. We first optimize all the nine parameters to obtain a minimum χ^2, χ^2_{min}; we then scan ϕ_2 from 0° to 180° optimizing the other eight parameters, whose resultant minima are defined as $\chi^2(\phi_2)$; the difference $\Delta\chi^2(\phi_2)$ is defined as $\Delta\chi^2(\phi_2) \equiv \chi^2(\phi_2) - \chi^2_{\text{min}}$. Performing a toy MC study following the procedure described in Ref. [42], we obtain the $1 - $ C.L. plot in Fig. 12 (dotted line) from the $\Delta\chi^2(\phi_2)$ [43].

In addition to the 26 observables obtained from our time-dependent Dalitz plot analysis, we use the branching fraction $\mathcal{B}(B^0 \rightarrow \rho\pi^{\text{all}})$ obtained in Sec. VIII and the following world average branching fractions and asymmetries: $\mathcal{B}(B^+ \rightarrow \rho^+\pi^0)$, $\mathcal{A}(B^+ \rightarrow \rho^+\pi^0)$, $\mathcal{B}(B^+ \rightarrow \rho^0\pi^+)$, and $\mathcal{A}(B^+ \rightarrow \rho^0\pi^+)$ [30], which are not correlated with our 26 observables. With the 31 measurements above, we perform a full combined Dalitz and isospin (pentagon) analysis. Having five related decay modes, we have 12 free parameters including ϕ_2:

$$12 = (10 \text{ complex amplitudes} = 20 \text{ d.o.f.}) + \phi_2$$
$$- (1 \text{ global phase}) - (4 \text{ isospin relations} = 8 \text{ d.o.f.}).$$
$$(65)$$

The detail of the χ^2 construction can be found in Appendix D. The χ^2_{min} obtained is 10.2, which is reasonable for $31(\text{measurements}) - 12(\text{free parameters}) = 19$ degrees of freedom. Following the same procedure as above, we obtain the $1 - $ C.L. plot in Fig. 12 (solid line).
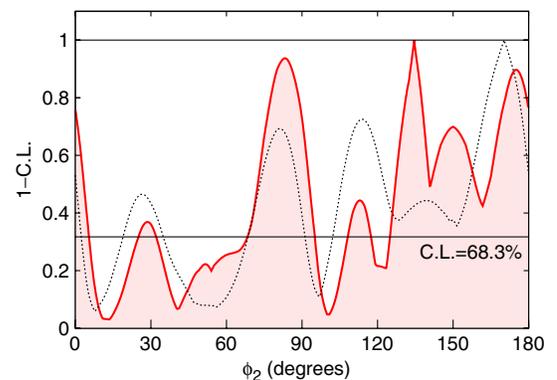
FIG. 12 (color online). $1 - $ C.L. vs ϕ_2. Dotted and solid curves correspond to the result from the time-dependent Dalitz plot analysis only and that from the Dalitz and an isospin (pentagon) combined analysis, respectively.

We obtain $68° < \phi_2 < 95°$ as the 68.3% confidence interval consistent with the SM expectation. Several SM-disfavored regions ($0° < \phi_2 < 5°$, $25° < \phi_2 < 32°$, and $108° < \phi_2 < 180°$) are also allowed.

X. CONCLUSION

Using 414 fb^{-1} of data we have performed a time-dependent Dalitz plot analysis of the $B^0 \to \pi^+ \pi^- \pi^0$ decay mode. Combining our analysis and information from charged B decay modes, a full Dalitz plot and isospin analysis is performed to obtain a constraint on ϕ_2 in a model-independent way. We obtain $68° < \phi_2 < 95°$ at the 68.3% confidence interval for the solution consistent with the SM expectation. However, a large CKM-disfavored region also remains. In principle, with more data we may be able to remove all the additional ϕ_2 solutions. From the result of the Dalitz plot analysis, we also obtain the branching fractions for the decays $B^0 \to \rho^\pm(770)\pi^\mp$ and $B^0 \to \rho^0(770)\pi^0$. These are the first branching fraction measurements of these processes with the lowest resonance $\rho(770)$ explicitly separated from the radial excitations.

APPENDIX A: PDFS FOR TIME-DEPENDENT DALITZ PLOT ANALYSIS

In this section, we describe the details of the PDF for each component that appears in Eq. (31).

1. Signal PDF

The PDF for signal events consists of a PDF for the correctly reconstructed events $\mathcal{P}_{\text{true}}$ and PDFs for SCF events $\mathcal{P}_i$ ($i = $ NR, CR):

$$\mathcal{P}_{\text{sig}}(\vec{x}) = \frac{\mathcal{P}_{\text{true}}(\vec{x}) + \sum\limits_{i=\text{NR,CR}} \mathcal{P}_i(\vec{x})}{\mathcal{N}_{\text{true}} + \sum\limits_{i=\text{NR,CR}} \mathcal{N}_i}, \quad (A1)$$

where NR and CR represent the π^0 (neutral) replaced and $\pi^\pm$ (charged) replaced SCF's, respectively, and $\mathcal{N}$ are the integrals of the PDF's.

a. PDF for correctly reconstructed events

In terms of the event fractions for the lth flavor-tagging region ($\mathcal{F}^l_{\text{true}}$), the Dalitz-plot-dependent efficiency (ϵ^l), the π^0 momentum-dependent efficiency correction taking account of the difference between data and MC simulation (ϵ'), wrong-tag fractions (w_l), and the differences in wrong-tag fractions between B^0 and $\overline{B}^0$ (Δw_l), the PDF for correctly reconstructed events is given by

$$\begin{aligned}\mathcal{P}_{\text{true}}(\vec{x}) = &\mathcal{F}^l_{\text{true}} \cdot \mathcal{P}_{\text{true}}(\Delta E, M_{\text{bc}}; p_{\pi^0})\\ &\cdot \epsilon_{\text{true}}(m', \theta'; l)\epsilon'(p_{\pi^0}) \cdot |\det J(m', \theta')|\\ &\cdot \mathcal{P}_{\text{true}}(m', \theta'; \Delta t, q_{\text{tag}}; l),\end{aligned} \quad (A2)$$

where the Dalitz-Δt PDF $\mathcal{P}_{\text{true}}(m', \theta'; \Delta t, q_{\text{tag}}; l)$ corresponds to the right-hand side of Eq. (11) and is

$$\begin{aligned}&\mathcal{P}_{\text{true}}(m', \theta'; \Delta t, q_{\text{tag}}; l)\\ &= \frac{e^{-|\Delta t|/\tau_{B^0}}}{4\tau_{B^0}}\Big\{(1 - q_{\text{tag}}\Delta w_1)(|A_{3\pi}|^2 + |\overline{A}_{3\pi}|^2)\\ &\quad - q_{\text{tag}}(1 - 2w_l)(|A_{3\pi}|^2 - |\overline{A}_{3\pi}|^2)\cos(\Delta m_d \Delta t)\\ &\quad + q_{\text{tag}}(1 - 2w_l)2\,\text{Im}\Big(\frac{q}{p}\overline{A}_{3\pi}A^*_{3\pi}\Big)\sin(\Delta m_d \Delta t)\Big\}.\end{aligned} \quad (A3)$$

For the Δt PDF, the above equation is convolved with the resolution function [23]. The terms $|A_{3\pi}|^2 \pm |\overline{A}_{3\pi}|^2$ and $\text{Im}(\frac{q}{p}\overline{A}_{3\pi}A^*_{3\pi})$ are expanded as in Eqs. (20) and (21). The ΔE-M_{bc} PDF is normalized such that

$$\iint_{\text{signal region}} d\Delta E dM_{\text{bc}} \mathcal{P}_{\text{true}}(\Delta E, M_{\text{bc}}; p_{\pi^0}) = 1 \quad (\forall p_{\pi^0}),$$
$$(A4)$$

since we define the Dalitz plot efficiency for events inside the signal region. Since the PDF's in the Δt-q_{tag} direction are also normalized to be unity, the integral inside the signal region, $\mathcal{N}_{\text{true}}$, is

$$\mathcal{N}_{\text{true}} = \sum_l \mathcal{N}^l_{\text{true}}, \quad (A5)$$

where

$$\mathcal{N}_{\text{true}}^{l} \equiv \sum_{q_{\text{tag}}} \int d\Delta t \iint_{\text{signal region}} d\Delta E dM_{\text{bc}} \iint_{\text{SDP,Veto}} dm' d\theta' \mathcal{P}_{\text{true}}(\vec{x})$$

$$= \mathcal{F}_{\text{true}}^{l} \iint_{\text{SDP,Veto}} dm' d\theta' \epsilon_{\text{true}}(m', \theta'; l) \epsilon'(p_{\pi^0}) |\det \boldsymbol{J}| (|A_{3\pi}|^2 + |\overline{A}_{3\pi}|^2), \tag{A6}$$

and the correlation between p_{π^0} and m' is properly taken into account in the integration on the last line. The notation $\iint_{\text{SDP,Veto}} dm' d\theta'$ means integration over the square Dalitz plot with the vetoed region in the Dalitz plot taken into account.

The π^0 momentum-dependent ΔE-M_{bc} PDF, $\mathcal{P}_{\text{true}}(\Delta E, M_{\text{bc}}; p_{\pi^0})$, is modeled using MC-simulated events in a binned histogram interpolated in the p_{π^0} direction, to which a small correction obtained with $\overline{B}^0 \to \rho^- D^{(*)+}$ is applied to account for the difference between data and MC simulation.

The Dalitz plot distribution is smeared and distorted by detection efficiencies and detector resolutions. We obtain the signal Dalitz plot efficiency from MC simulation to take the former into account. We introduce a dependence of the efficiency on the r region, $\epsilon_{\text{true}}^{l}$, since a significant dependence is observed in MC simulation. Small corrections, $\epsilon'(p_{\pi^0})$, are also applied to the MC-determined efficiency to account for differences between data and MC simulation. We use $\overline{B}^0 \to \rho^- D^{(*)+}$, $\overline{B}^0 \to \pi^- D^{*-}$, $B^- \to \rho^- D^0$, and $B^- \to \pi^- D^0$ decays to obtain the correction factors. The smearing in the Dalitz plot due to the finite detector resolutions is small compared to the widths of $\rho(770)$ resonances; the smearing is confirmed by MC to be a negligibly small effect.

b. PDF for SCF events

Approximately 20% of signal candidates are SCFs, which are subdivided into ~4% NR SCF and ~16% CR SCF. It is therefore important to develop a model that describes the SCF component well. The time-dependent PDF for SCF events is defined as

$$\mathcal{P}_i(\Delta E, M_{\text{bc}}; m', \theta'; \Delta t, q_{\text{tag}}; l) = \mathcal{F}_i^l \cdot \mathcal{P}_i(\Delta E, M_{\text{bc}}; s_i)$$
$$\cdot \mathcal{P}_i(m', \theta'; \Delta t, q_{\text{tag}})$$
$$(i = \text{NR, CR}), \tag{A7}$$

with

$$\mathcal{P}_i(m', \theta'; \Delta t, q_{\text{tag}}) = \frac{e^{-|\Delta t|/\tau_i}}{4\tau_i} \{(1 - q_{\text{tag}} \Delta w_l^i) \mathcal{P}_i^{\text{life}}(m', \theta')$$
$$- q_{\text{tag}}(1 - 2w_l^i) \mathcal{P}_i^{\cos}(m', \theta')$$
$$\times \cos(\Delta m_d \Delta t)$$
$$+ q_{\text{tag}}(1 - 2w_l^i) \mathcal{P}_i^{\sin}(m', \theta')$$
$$\times \sin(\Delta m_d \Delta t)\}, \tag{A8}$$

where $\mathcal{F}_i^l$ is the event fraction in each tagging r bin.

The ΔE-M_{bc} PDF is normalized inside the signal region as

$$\iint_{\text{signal region}} d\Delta E dM_{\text{bc}} \mathcal{P}_i(\Delta E, M_{\text{bc}}; s_i) = 1 \quad (\forall \ s_i). \tag{A9}$$

As the PDF's in the Δt-q_{tag} direction are normalized to unity and $\sum_l \mathcal{F}_i^l = 1$, the integral inside the signal region, $\mathcal{N}_i$, is

$$\mathcal{N}_i \equiv \sum_l \sum_{q_{\text{tag}}} \int d\Delta t \iint_{\text{signal region}} d\Delta E dM_{\text{bc}} \iint_{\text{SDP,Veto}} dm' d\theta' \mathcal{P}_i^l(\Delta E, M_{\text{bc}}; m', \theta'; \Delta t, q_{\text{tag}})$$

$$= \iint_{\text{SDP,Veto}} dm' d\theta' \mathcal{P}_i^{\text{life}}(m', \theta'). \tag{A10}$$

We find that the ΔE-M_{bc} distribution for SCF has a sizable correlation with Dalitz plot variables, but only in one of its two dimensions. We thus introduce a model with dependences on the Dalitz plot variable s_i. The variable $s_{\text{CR}} = s_\pm \equiv \max(s_+, s_-)$ is used, because the CR SCF can be divided into a π^+ replaced SCF and a π^- replaced SCF, where s_- (s_+) is used for π^+ (π^-) replaced SCF. Here, we exploit the fact that almost all of the π^+ (π^-) replaced SCF distributes in the region of $s_+ < s_-$ ($s_+ > s_-$). For the NR SCF, $s_{\text{NR}} = s_0$. This parametrization models the correlation quite well, with each of the parameters s_i related to the kinematics of replaced tracks.

Since track (π) replacement changes the measured kinematic variables, the SCF events "migrate" in the Dalitz plot from the correct (or generated) position to the observed position. Using MC simulation, we determine resolution functions $R_i(m'_{\text{obs}}, \theta'_{\text{obs}}; m'_{\text{gen}}, \theta'_{\text{gen}})$ to describe this "migration" effect, where $(m'_{\text{obs}}, \theta'_{\text{obs}})$ and $(m'_{\text{gen}}, \theta'_{\text{gen}})$ are the observed and the generated (correct) positions in the Dalitz plot, respectively. The resolution function satisfies the normalization condition of

$$\iint_{\text{SDP}} dm'_{\text{obs}} d\theta'_{\text{obs}} R_i(m'_{\text{obs}}, \theta'_{\text{obs}}; m'_{\text{gen}}, \theta'_{\text{gen}}) = 1$$
$$(\forall \ m'_{\text{gen}}, \theta'_{\text{gen}}). \tag{A11}$$

Together with the efficiency function $\epsilon_i(m'_{\text{gen}}, \theta'_{\text{gen}})$, which is also obtained with MC simulation, the Dalitz plot PDF for SCF is described as

$$
\begin{aligned}
\mathcal{P}_i^j(m', \theta') &= [(R_i \cdot \epsilon_i) \otimes P_{\text{phys}}^j](m', \theta') \\
&\equiv \iint_{\text{SDP}} dm'_{\text{gen}} d\theta'_{\text{gen}} R_i(m', \theta'; m'_{\text{gen}}, \theta'_{\text{gen}}) \\
&\quad \cdot \epsilon_i(m'_{\text{gen}}, \theta'_{\text{gen}}) \cdot P_{\text{phys}}^j(m'_{\text{gen}}, \theta'_{\text{gen}}), \\
&\quad (i = \text{CR, NR}, \ j = \text{life, cos, sin})
\end{aligned} \tag{A12}
$$

where

$$
\begin{aligned}
P_{\text{phys}}^{\text{life}}(m'_{\text{gen}}, \theta'_{\text{gen}}) &= |\det \mathbf{J}|(|A_{3\pi}|^2 + |\overline{A}_{3\pi}|^2), \\
P_{\text{phys}}^{\text{cos}}(m'_{\text{gen}}, \theta'_{\text{gen}}) &= |\det \mathbf{J}|(|A_{3\pi}|^2 - |\overline{A}_{3\pi}|^2), \\
P_{\text{phys}}^{\text{sin}}(m'_{\text{gen}}, \theta'_{\text{gen}}) &= |\det \mathbf{J}| 2 \operatorname{Im}\left(\frac{q}{p} \overline{A}_{3\pi} A_{3\pi}^*\right).
\end{aligned} \tag{A13}
$$

For the NR SCF, the shape of the Δt PDF defined in Eq. (A8) is exactly the same as the correctly reconstructed signal, i.e., $\tau_{\text{NR}} = \tau_{B^0}$, $w_l^{\text{NR}} = w_l$, and $\Delta w_l^{\text{NR}} = \Delta w_l$, since the replaced π^0 is not used for either vertexing or flavor tagging. On the other hand, for the CR SCF, the Δt PDF is different from correctly reconstructed signal, since the replaced $\pi^\pm$ is used for both vertexing and flavor tagging. Thus, we use MC-simulated CR SCF events to obtain τ_{CR}, w_l^{CR}, and Δw_l^{CR}, which are different from those of correctly reconstructed signal events. In particular, Δw_l^{CR} is opposite in sign for the π^+ and π^- replaced SCFs, due to the fact that the replaced $\pi^\pm$ tends to be directly used for flavor tagging in the slow pion category.

2. Continuum PDF

The PDF for the continuum background is

$$
\begin{aligned}
\mathcal{P}_{q\bar{q}}&(\Delta E, M_{\text{bc}}; m', \theta'; \Delta t, q_{\text{tag}}; l) \\
&= \mathcal{F}_{q\bar{q}}^l \cdot \mathcal{P}_{q\bar{q}}^l(\Delta E, M_{\text{bc}}) \cdot \mathcal{P}_{q\bar{q}}(m', \theta'; \Delta E, M_{\text{bc}}) \\
&\quad \cdot \left[\frac{1 + q_{\text{tag}} A^l(m', \theta')}{2}\right] \cdot \mathcal{P}_{q\bar{q}}(\Delta t),
\end{aligned} \tag{A14}
$$

where $\mathcal{F}_{q\bar{q}}^l$ is the event fraction for each r region obtained in the signal yield fit. All the terms on the right-hand side of the equation are normalized to be unity so that

$$
\begin{aligned}
\sum_l \sum_{q_{\text{tag}}} \int d\Delta t &\iint_{\text{signal region}} d\Delta E dM_{\text{bc}} \iint_{\text{SDP,Veto}} dm' d\theta' \\
&\times \mathcal{P}_{q\bar{q}}(\Delta E, M_{\text{bc}}; m', \theta'; \Delta t, q_{\text{tag}}; l) = 1.
\end{aligned} \tag{A15}
$$

Since the allowed kinematic region is dependent on ΔE and M_{bc}, the Dalitz plot distribution is dependent on ΔE and M_{bc}. We define a ΔE-M_{bc}-independent PDF, $\mathcal{P}_{q\bar{q}}(m'_{\text{scale}}, \theta')$, where m'_{scale} is a redefined SDP variable with the kinematic effect taken into account as

$$
m'_{\text{scale}} \equiv \frac{1}{\pi} \arccos\left(2 \frac{m_0 - m_0^{\text{min}}}{m_0^{\text{max}} - m_0^{\text{min}} + \Delta E + \Delta M_{\text{bc}}} - 1\right), \tag{A16}
$$

where

$$
\Delta M_{\text{bc}} \equiv M_{\text{bc}} - m_{B^0}. \tag{A17}
$$

Using the ΔE-M_{bc}-independent PDF, $\mathcal{P}_{q\bar{q}}(m', \theta'; \Delta E, M_{\text{bc}})$ is described as

$$
\begin{aligned}
\mathcal{P}_{q\bar{q}}(m', \theta'; \Delta E, M_{\text{bc}}) &= \frac{1}{\mathcal{N}_{q\bar{q}}(\Delta E + \Delta M_{\text{bc}})} \\
&\quad \cdot \frac{\sin(\pi m')}{\sin(\pi m'_{\text{scale}})} \cdot \mathcal{P}_{q\bar{q}}(m'_{\text{scale}}, \theta')
\end{aligned} \tag{A18}
$$

for the region, $m_0^{\text{min}} < m_0 < \min(m_0^{\text{max}}, m_0^{\text{max}} + \Delta E + \Delta M_{\text{bc}})$ ($p_{q\bar{q}} = 0$ otherwise), where $\mathcal{N}_{q\bar{q}}(\Delta E + \Delta M_{\text{bc}})$ and $\sin(\pi m')/\sin(\pi m'_{\text{scale}})$ are the normalization factor and the Jacobian for the parameter transformation $m'_{\text{scale}} \to m'$, respectively. We obtain the $p_{q\bar{q}}(m'_{\text{scale}}, \theta')$ distribution from data in part of the sideband region, $-0.1 \text{ GeV} < \Delta E < 0.2 \text{ GeV}$ and $5.2 \text{ GeV}/c^2 < M_{\text{bc}} < 5.26 \text{ GeV}/c^2$, where the contribution from $B\overline{B}$ background is negligible.

Since we find significant flavor asymmetry depending on the location in the Dalitz plot, we introduce the following term to take account of it:

$$
\frac{1 + q_{\text{tag}} A^l(m', \theta')}{2}, \tag{A19}
$$

which is r-region dependent. The asymmetry is antisymmetric in the direction of θ', i.e., $A^l(m', \theta') > 0$ [$A^l(m', \theta') < 0$] in the region of $\theta' > 0.5$ ($\theta < 0.5$), and the size of the asymmetry is at most $\sim 20\%$ in the best r region. This effect is due to the jetlike topology of continuum events; when an event has a high momentum π^- (π^+) on the *CP* side, the highest momentum π on the tag side tends to have $+$ ($-$) charge. The highest momentum π on the tag side with $+$ ($-$) charge tags the flavor as B^0 ($\overline{B}^0$). Since an event with a high momentum π^- (π^+) resides in the region $\theta' > 0.5$ ($\theta' < 0.5$), a continuum event in the region $\theta' > 0.5$ ($\theta' < 0.5$) tends to be tagged as B^0 ($\overline{B}^0$). We again parametrize the asymmetry $A^l(m', \theta')$ in a ΔE-M_{bc}-independent way as

$$
A^l(m', \theta') = A^l(m', \theta'; \Delta E, M_{\text{bc}}) = A^l(m'_{\text{scale}}, \theta'), \tag{A20}
$$

and model it with a two-dimensional polynomial, whose coefficients are determined by a fit to data in the ΔE-M_{bc} sideband region.

3. $B\overline{B}$ background PDF

The treatment of $B\overline{B}$ background is different for *CP* eigenstate modes and flavor-specific or charged modes. The PDF for the *CP* eigenstate modes is

$$\mathcal{P}^l_{B\overline{B}}(\Delta E, M_{\mathrm{bc}}; m', \theta'; \Delta t, q_{\mathrm{tag}})$$
$$= \mathcal{F}^l_{B\overline{B}} \cdot \mathcal{P}_{B\overline{B}}(\Delta E, M_{\mathrm{bc}}) \cdot \mathcal{P}_{B\overline{B}}(m', \theta') \cdot \mathcal{P}_{B\overline{B}}(\Delta t, q_{\mathrm{tag}}; l),$$

(A21)

where $\mathcal{P}_{B\overline{B}}(\Delta t, q_{\mathrm{tag}})$ is a time-dependent *CP* violation PDF normalized as

$$\sum_{q_{\mathrm{tag}}} \int d\Delta t \mathcal{P}_{B\overline{B}}(\Delta t, q_{\mathrm{tag}}; l) = 1 \quad (\forall \, l). \tag{A22}$$

For the flavor-specific or charged modes, the PDF is

$$\mathcal{P}_{B\overline{B}}(\Delta E, M_{\mathrm{bc}}; m', \theta'; \Delta t, q_{\mathrm{tag}}; l)$$
$$= \mathcal{F}^l_{B\overline{B}} \cdot \mathcal{P}_{B\overline{B}}(\Delta E, M_{\mathrm{bc}})$$
$$\times \sum_{q_{\mathrm{rec}}} \mathcal{P}_{B\overline{B}}(m', \theta'; q_{\mathrm{rec}}) \cdot \mathcal{P}_{B\overline{B}}(\Delta t, q_{\mathrm{tag}}, q_{\mathrm{rec}}; l), \tag{A23}$$

where the Dalitz plot PDF $\mathcal{P}_{B\overline{B}}(m', \theta'; q_{\mathrm{rec}})$ is dependent on the true flavor of the *CP* (fully reconstructed) side, q_{rec}, and the time-dependent part is a mixing PDF (lifetime PDF with flavor asymmetry) for flavor-specific (charged) modes. The Δt PDF is normalized as

$$\sum_{q_{\mathrm{tag}}} \sum_{q_{\mathrm{rec}}} \int d\Delta t \mathcal{P}_{B\overline{B}}(\Delta t, q_{\mathrm{tag}}, q_{\mathrm{rec}}; l) = 1 \quad (\forall \, l). \tag{A24}$$

The ΔE-M_{bc} PDF and Dalitz plot PDF are obtained mode by mode from MC simulation. The Dalitz plot PDF of the *CP* eigenstate modes is assumed to have the following symmetry,

$$\mathcal{P}_{B\overline{B}}(m', \theta') = \mathcal{P}_{B\overline{B}}(m', 1 - \theta'), \tag{A25}$$

while that of flavor-specific and charged modes is assumed to have the following symmetry,

$$\mathcal{P}_{B\overline{B}}(m', \theta'; q_{\mathrm{rec}}) = \mathcal{P}_{B\overline{B}}(m', 1 - \theta'; -q_{\mathrm{rec}}). \tag{A26}$$

The total PDF of the $B\overline{B}$ background is a linear combination of each mode with efficiencies and branching fractions taken into account.

APPENDIX B: CORRELATION MATRIX OF THE FIT RESULT

Tables IX, X, and XI show the correlation matrix for the 26 parameters determined in the time-dependent Dalitz plot analysis, corresponding to the total error matrix with

TABLE IX. Correlation matrix (1) of the 26 fitted parameters, with statistical and systematic errors combined.

	U_-^+	U_0^+	$U_{+-}^{+,\mathrm{Re}}$	$U_{+0}^{+,\mathrm{Re}}$	$U_{-0}^{+,\mathrm{Re}}$	$U_{+-}^{+,\mathrm{Im}}$	$U_{+0}^{+,\mathrm{Im}}$	$U_{-0}^{+,\mathrm{Im}}$
U_-^+	$+1.00$							
U_0^+	$+0.22$	$+1.00$						
$U_{+-}^{+,\mathrm{Re}}$	$+0.06$	$+0.04$	$+1.00$					
$U_{+0}^{+,\mathrm{Re}}$	$+0.10$	$+0.02$	$+0.02$	$+1.00$				
$U_{-0}^{+,\mathrm{Re}}$	-0.04	-0.11	$+0.01$	$+0.01$	$+1.00$			
$U_{+-}^{+,\mathrm{Im}}$	$+0.08$	$+0.03$	$+0.12$	$+0.02$	-0.00	$+1.00$		
$U_{+0}^{+,\mathrm{Im}}$	-0.03	-0.08	-0.00	$+0.13$	$+0.02$	-0.00	$+1.00$	
$U_{-0}^{+,\mathrm{Im}}$	-0.14	-0.08	-0.02	-0.02	$+0.10$	-0.01	$+0.01$	$+1.00$
U_+^-	$+0.05$	$+0.02$	$+0.00$	-0.02	$+0.00$	-0.02	-0.01	-0.01
U_-^-	-0.23	-0.08	-0.03	-0.04	-0.02	-0.03	$+0.01$	$+0.03$
U_0^-	$+0.05$	$+0.10$	$+0.01$	$+0.00$	-0.04	$+0.01$	-0.06	-0.08
$U_{+-}^{-,\mathrm{Re}}$	-0.03	-0.01	-0.03	-0.00	-0.00	-0.04	$+0.00$	$+0.01$
$U_{+0}^{-,\mathrm{Re}}$	-0.04	-0.01	-0.01	-0.12	-0.00	$+0.00$	-0.01	$+0.02$
$U_{-0}^{-,\mathrm{Re}}$	-0.02	-0.04	-0.00	-0.00	$+0.06$	-0.00	$+0.01$	$+0.08$
$U_{+-}^{-,\mathrm{Im}}$	-0.04	-0.02	-0.05	-0.01	-0.00	$+0.00$	$+0.00$	$+0.01$
$U_{+0}^{-,\mathrm{Im}}$	-0.03	-0.09	-0.01	-0.01	$+0.02$	-0.00	-0.04	$+0.01$
$U_{-0}^{-,\mathrm{Im}}$	$+0.01$	-0.02	$+0.00$	$+0.00$	$+0.00$	-0.00	$+0.00$	-0.25
I_+	$+0.00$	$+0.00$	-0.02	-0.01	-0.00	-0.05	-0.01	-0.00
I_-	$+0.06$	$+0.03$	-0.01	$+0.01$	-0.02	$+0.05$	-0.00	$+0.04$
I_0	$+0.01$	$+0.01$	$+0.00$	$+0.02$	-0.00	$+0.00$	-0.02	-0.02
I_{+-}^{Re}	-0.04	-0.01	$+0.01$	-0.00	$+0.00$	-0.16	$+0.00$	$+0.00$
I_{+0}^{Re}	$+0.00$	$+0.02$	$+0.00$	-0.13	-0.01	-0.00	-0.00	-0.00
I_{-0}^{Re}	-0.06	$+0.01$	-0.01	-0.01	-0.12	$+0.00$	-0.01	-0.29
I_{+-}^{Im}	-0.02	-0.01	$+0.13$	-0.00	$+0.00$	$+0.00$	$+0.00$	$+0.00$
I_{+0}^{Im}	-0.01	-0.03	$+0.00$	$+0.00$	$+0.01$	$+0.01$	$+0.04$	$+0.01$
I_{-0}^{Im}	-0.06	-0.04	-0.01	-0.02	-0.09	-0.02	$+0.01$	$+0.08$

TABLE X. Correlation matrix (2) of the 26 fitted parameters, with statistical and systematic errors combined.

	U_+^-	U_-^-	U_0^-	$U_{+-}^{-,\mathrm{Re}}$	$U_{+0}^{-,\mathrm{Re}}$	$U_{-0}^{-,\mathrm{Re}}$	$U_{+-}^{-,\mathrm{Im}}$	$U_{+0}^{-,\mathrm{Im}}$	$U_{-0}^{-,\mathrm{Im}}$
U_+^-	+1.00								
U_-^-	−0.06	+1.00							
U_0^-	+0.00	−0.01	+1.00						
$U_{+-}^{-,\mathrm{Re}}$	−0.07	+0.01	−0.00	+1.00					
$U_{+0}^{-,\mathrm{Re}}$	−0.21	+0.03	−0.08	+0.02	+1.00				
$U_{-0}^{-,\mathrm{Re}}$	+0.01	−0.12	−0.16	−0.00	+0.02	+1.00			
$U_{+-}^{-,\mathrm{Im}}$	+0.03	+0.03	−0.00	+0.20	−0.01	−0.00	+1.00		
$U_{+0}^{-,\mathrm{Im}}$	−0.02	+0.01	−0.03	+0.00	+0.01	+0.01	+0.00	+1.00	
$U_{-0}^{-,\mathrm{Im}}$	+0.00	−0.03	+0.02	−0.00	−0.00	+0.14	−0.00	+0.01	+1.00
I_+	−0.02	−0.01	+0.00	+0.03	+0.01	+0.00	−0.02	+0.01	+0.00
I_-	−0.00	−0.01	+0.01	+0.03	−0.00	−0.05	+0.00	−0.01	−0.07
I_0	+0.00	−0.01	+0.07	−0.00	−0.02	+0.02	−0.00	−0.05	−0.06
I_{+-}^{Re}	+0.02	+0.01	−0.00	−0.02	−0.00	+0.00	−0.15	+0.00	+0.00
I_{+0}^{Re}	−0.01	+0.00	+0.02	+0.00	+0.09	−0.01	−0.00	+0.16	+0.01
I_{-0}^{Re}	−0.01	+0.08	+0.08	+0.01	−0.00	−0.12	+0.01	−0.00	+0.21
I_{+-}^{Im}	+0.02	+0.04	−0.00	+0.04	−0.00	−0.00	+0.04	+0.00	−0.00
I_{+0}^{Im}	+0.03	+0.00	−0.03	−0.01	−0.28	+0.00	+0.01	−0.03	+0.01
I_{-0}^{Im}	−0.00	+0.01	−0.01	−0.00	+0.01	+0.18	+0.00	+0.02	+0.11

TABLE XI. Correlation matrix (3) of the 26 fitted parameters, with statistical and systematic errors combined.

	I_+	I_-	I_0	I_{+-}^{Re}	I_{+0}^{Re}	I_{-0}^{Re}	I_{+-}^{Im}	I_{+0}^{Im}	I_{-0}^{Im}
I_+	+1.00								
I_-	−0.06	+1.00							
I_0	+0.00	+0.01	+1.00						
I_{+-}^{Re}	−0.04	−0.06	−0.00	+1.00					
I_{+0}^{Re}	+0.04	−0.00	−0.14	−0.00	+1.00				
I_{-0}^{Re}	−0.02	+0.21	+0.01	−0.01	+0.00	+1.00			
I_{+-}^{Im}	−0.07	−0.01	−0.00	−0.35	−0.00	+0.00	+1.00		
I_{+0}^{Im}	−0.15	+0.01	−0.09	+0.01	−0.23	−0.00	+0.01	+1.00	
I_{-0}^{Im}	+0.01	−0.14	−0.23	+0.01	+0.04	−0.06	+0.00	+0.03	+1.00

statistical and systematic error matrices combined. We assume no correlations for the systematic errors.

APPENDIX C: FORMALISM FOR BRANCHING FRACTION MEASUREMENT

In this section, we describe the formalism for the factors used in the branching fraction calculation of Eqs. (60) and (61).

1. Detection efficiency

Since the detection efficiency is Dalitz-plot dependent, we use the detection efficiency averaged over the Dalitz plot, ϵ^{Det}, for the branching fraction measurement. From Eqs. (A1)–(A3), (A7), (A8), and (A12), the PDF integrated over ΔE-M_{bc} (in the signal region) and Δt, and summed over q_{tag} and l, is

$$\mathcal{P}_{\mathrm{sig}}(m', \theta') = \frac{\mathcal{P}_{\mathrm{true}}(m', \theta') + \sum_{i=\mathrm{CR,NR}} \mathcal{P}_i(m', \theta')}{\mathcal{N}_{\mathrm{true}} + \sum_{i=\mathrm{CR,NR}} \mathcal{N}_i}, \quad (\mathrm{C1})$$

with

$$\mathcal{P}_{\mathrm{true}}(m', \theta') = \sum_l \mathcal{F}_{\mathrm{true}}^l \epsilon_{\mathrm{true}}(m', \theta'; l) \epsilon'(p_{\pi^0}) P_{\mathrm{phys}}(m', \theta'),$$

$$(\mathrm{C2})$$

$$\mathcal{P}_i(m', \theta') = \sum_l \mathcal{F}_i^l [(\epsilon_i \cdot R_i) \otimes P_{\mathrm{phys}}](m', \theta'), \quad (\mathrm{C3})$$

and

$$P_{\text{phys}}(m', \theta')$$
$$= |\boldsymbol{J}(m', \theta')|(|A_{3\pi}|^2 + |\overline{A}_{3\pi}|^2)$$
$$= |\boldsymbol{J}(m', \theta')|\left\{\sum_\kappa U_\kappa^+ |f_\kappa|^2\right.$$
$$\left. + \sum_{\kappa < \sigma} (U_{\kappa\sigma}^{+,\text{Re}} \text{Re}[f_\kappa f_\sigma^*] - U_{\kappa\sigma}^{+,\text{Im}} \text{Im}[f_\kappa f_\sigma^*])\right\}. \quad (C4)$$

Consequently, $\mathcal{P}_{\text{sig}}(m', \theta')$ can be symbolically rewritten as

$$\mathcal{P}_{\text{sig}}(m', \theta') = \frac{[\epsilon^{\text{sig}} \otimes P_{\text{phys}}](m', \theta')}{\mathcal{N}_{\text{true}} + \sum_{i=\text{CR,NR}} \mathcal{N}_i}, \quad (C5)$$

where

$$[\epsilon^{\text{sig}} \otimes P_{\text{phys}}](m', \theta')$$
$$\equiv \sum_l \mathcal{F}_{\text{true}}^l \epsilon_{\text{true}}(m', \theta'; l) \epsilon'(p_{\pi^0}) P_{\text{phys}}(m', \theta')$$
$$+ \sum_{i=\text{CR,NR}} \sum_l \mathcal{F}_i^l [(\epsilon_i \cdot R_i) \otimes P^{\text{phys}}](m', \theta'). \quad (C6)$$

Note that R_i is normalized as Eq. (A11).

Consequently, the detection efficiency averaged over the Dalitz plot ϵ^{Det} is

$$\epsilon^{\text{Det}} = \frac{\iint_{\text{SDP,Veto}} dm' d\theta' [\epsilon^{\text{sig}} \otimes P^{\text{phys}}](m', \theta')}{\iint_{\text{SDP,Veto}} dm' d\theta' P^{\text{phys}}(m', \theta')} \quad (C7)$$

$$= \frac{\mathcal{N}_{\text{true}} + \sum_{i=\text{CR,NR}} \mathcal{N}_i}{\iint_{\text{SDP,Veto}} dm' d\theta' P^{\text{phys}}(m', \theta')}. \quad (C8)$$

2. Dalitz veto efficiency

The efficiency corresponding to the Dalitz veto, ϵ^{Veto}, is simply calculated as

$$\epsilon^{\text{Veto}} = \frac{\iint_{\text{SDP,Veto}} dm' d\theta' P_{\text{phys}}(m', \theta')}{\iint_{\text{SDP,Whole}} dm' d\theta' P_{\text{phys}}(m', \theta')}. \quad (C9)$$

3. Fraction of $\rho_{\text{all}}^\kappa \pi^\sigma$

The fraction of $B^0 \to \rho_{\text{all}}^\kappa \pi^\sigma$ normalized to $B^0 \to \pi^+ \pi^- \pi^0$ is

$$f_{\rho_{\text{all}}^\kappa} = \frac{\iint_{\text{SDP,Whole}} dm' d\theta' P_{\text{all},\kappa}^{\text{phys}}(m', \theta')}{\iint_{\text{SDP,Whole}} dm' d\theta' P_{\text{phys}}(m', \theta')}, \quad (C10)$$

where

$$P_{\text{all},\kappa}^{\text{phys}}(m', \theta') = |\boldsymbol{J}(m', \theta')| U_\kappa^+ |f_\kappa|^2. \quad (C11)$$

4. Fraction of $\rho^\kappa(770)\pi^\sigma$

The fraction of $B^0 \to \rho^\kappa(770)\pi^\sigma$ normalized to $B^0 \to \rho_{\text{all}}^\kappa \pi^\sigma$ is

$$f_{\rho^\kappa(770)} = \frac{\iint_{\text{SDP,Whole}} dm' d\theta' P_{(770),\kappa}^{\text{phys}}(m', \theta')}{\iint_{\text{SDP,Whole}} dm' d\theta' P_{\text{all},\kappa}^{\text{phys}}(m', \theta')}, \quad (C12)$$

where

$$P_{(770),\kappa}^{\text{phys}}(m', \theta') = |\boldsymbol{J}(m', \theta')| U_\kappa^+ |f_\kappa^{\rho(770)}|^2. \quad (C13)$$

The function $f_\kappa^{\rho(770)}$ is defined as

$$f_\kappa^{\rho(770)} = T_{J=1}^\kappa \text{BW}_{\rho(770)}(s_\kappa), \quad (C14)$$

corresponding to the $\rho(770)$ part of f_κ defined in Eqs. (16) and (17).

5. Summary

By using the expressions described above, Eqs. (60) and (61) are rewritten as

$$\mathcal{B}(\rho \pi^{\text{all}}) = \frac{N_{\text{sig}}}{N_{B\overline{B}}} \frac{\iint_{\text{SDP,Whole}} dm' d\theta' P_{\text{phys}}(m', \theta')}{\mathcal{N}_{\text{true}} + \sum_{i=\text{CR,NR}} \mathcal{N}_i} \quad (C15)$$

and

$$\mathcal{B}(\rho^\kappa(770)\pi^\sigma) = \frac{N_{\text{sig}}}{N_{B\overline{B}}} \frac{\iint_{\text{SDP,Whole}} dm' d\theta' P_{(770),\kappa}^{\text{phys}}(m', \theta')}{\mathcal{N}_{\text{true}} + \sum_{i=\text{CR,NR}} \mathcal{N}_i}. \quad (C16)$$

APPENDIX D: METHOD OF ϕ_2 CONSTRAINT

1. Formalism

We define amplitudes as

$$A^+ \equiv A(B^0 \to \rho^+ \pi^-), \quad (D1)$$

$$A^- \equiv A(B^0 \to \rho^- \pi^+), \quad (D2)$$

$$A^0 \equiv A(B^0 \to \rho^0 \pi^0), \quad (D3)$$

$$A^{+0} \equiv A(B^+ \to \rho^+ \pi^0), \quad (D4)$$

$$A^{0+} \equiv A(B^+ \to \rho^0 \pi^+), \quad (D5)$$

and

$$\overline{A}^+ \equiv \frac{q}{p} A(\overline{B}^0 \to \rho^+ \pi^-), \quad (D6)$$

$$\overline{A}^- \equiv \frac{q}{p} A(\overline{B}^0 \to \rho^- \pi^+), \quad (D7)$$

$$\overline{A}^0 \equiv \frac{q}{p} A(\overline{B}^0 \to \rho^0 \pi^0), \quad (D8)$$

$$A^{-0} \equiv \frac{q}{p} A(B^- \to \rho^- \pi^0), \quad (D9)$$

$$A^{0-} \equiv \frac{q}{p} A(B^- \to \rho^0 \pi^-). \tag{D10}$$

These amplitudes are obtained from (i) 26 measurements determined in the time-dependent Dalitz plot analysis as well as (ii) branching fractions and asymmetry measurements, and give a constraint on ϕ_2.

Equations (22)–(25) define the relations between the amplitudes for the neutral modes and the parameters determined in the time-dependent Dalitz plot analysis. The relations between the branching fractions and asymmetries, and the amplitudes are

$$\mathcal{B}(\rho \pi^{\text{all}}) = c \cdot \sum_{\kappa=+,-,0} (|A^\kappa|^2 + |\overline{A}^\kappa|^2) \cdot \tau_{B^0}, \tag{D11}$$

$$\mathcal{B}(\rho^+ \pi^0) = c \cdot (|A^{+0}|^2 + |A^{-0}|^2) \cdot \tau_{B^+}, \tag{D12}$$

$$\mathcal{B}(\rho^0 \pi^+) = c \cdot (|A^{0+}|^2 + |A^{0-}|^2) \cdot \tau_{B^+}, \tag{D13}$$

$$\mathcal{A}(\rho^+ \pi^0) = \frac{|A^{-0}|^2 - |A^{+0}|^2}{|A^{-0}|^2 + |A^{+0}|^2}, \tag{D14}$$

$$\mathcal{A}(\rho^0 \pi^+) = \frac{|A^{0-}|^2 - |A^{0+}|^2}{|A^{0-}|^2 + |A^{0+}|^2}, \tag{D15}$$

where c is a constant and the lifetimes τ_{B^0} and τ_{B^+} are introduced to take account of the total width difference between B^0 and B^+. Note that we do not use quasi-two-body parameters related to neutral modes except for $\mathcal{B}(\rho^\pm \pi^\mp)$, since they are included in the Dalitz plot parameters.

The amplitudes are expected to follow $SU(2)$ isospin symmetry to a good approximation [7,8],

$$A^+ + A^- + 2A^0 = \tilde{A}^+ + \tilde{A}^- + 2\tilde{A}^0$$
$$= \sqrt{2}(A^{+0} + A^{0+})$$
$$= \sqrt{2}(\tilde{A}^{-0} + \tilde{A}^{0-}), \tag{D16}$$

$$A^{+0} - A^{0+} - \sqrt{2}(A^+ - A^-) = \tilde{A}^{-0} - \tilde{A}^{0-}$$
$$- \sqrt{2}(\tilde{A}^- - \tilde{A}^+), \tag{D17}$$

where

$$\tilde{A}^\kappa \equiv e^{-2i\phi_2}\overline{A}^\kappa,$$
$$\tilde{A}^{-0} \equiv e^{-2i\phi_2}A^{-0}, \quad \text{and} \quad \tilde{A}^{0-} \equiv e^{-2i\phi_2}A^{0-}. \tag{D18}$$

Note that there is an inconsistency in Eq. (D17) between Refs. [7,8]; we follow the treatment of Ref. [7].

2. Parametrization

Here we give two examples of the parametrization of the amplitudes. The first example may be more intuitive, while the second example is well behaved in the fit. The results are independent of the parametrizations with respect to the constraint on ϕ_2.

In the following, we set the constant c to be unity and discard the normalization condition $|A^+|^2 + |\overline{A}^+|^2 = 1$ instead. This is equivalent to letting c be a free parameter in the ϕ_2 constraint fit, keeping the normalization $|A^+|^2 + |\overline{A}^+|^2 = 1$. We adopt the former for simplicity. Note that Eqs. (22)–(25) become

$$U_\kappa^\pm = (|A^\kappa|^2 \pm |\overline{A}^\kappa|^2)/N,$$

$$I_\kappa = \text{Im}[\overline{A}^\kappa A^{\kappa*}]/N,$$

$$U_{\kappa\sigma}^{\pm,\text{Re(Im)}} = \text{Re(Im)}[A^\kappa A^{\sigma*} \pm \overline{A}^\kappa \overline{A}^{\sigma*}]/N,$$

$$I_{\kappa\sigma}^{\text{Re(Im)}} = \text{Re(Im)}[\overline{A}^\kappa A^{\sigma*} - (+)\overline{A}^\sigma A^{\kappa*}]/N$$

$$(N \equiv |A^+|^2 + |\overline{A}^+|^2)$$

in this case.

a. Amplitude parametrization

We can parametrize the amplitudes as follows [7]:

$$A^+ = e^{-i\phi_2}T^+ + P^+, \tag{D19}$$

$$A^- = e^{-i\phi_2}T^- + P^-, \tag{D20}$$

$$A^0 = e^{-i\phi_2}T^0 - \tfrac{1}{2}(P^+ + P^-), \tag{D21}$$

$$\sqrt{2}A^{+0} = e^{-i\phi_2}T^{+0} + P^+ - P^-, \tag{D22}$$

$$\sqrt{2}A^{0+} = e^{-i\phi_2}(T^+ + T^- + 2T^0 - T^{+0}) - P^+ + P^-, \tag{D23}$$

and

$$\overline{A}^+ = e^{+i\phi_2}T^- + P^-, \tag{D24}$$

$$\overline{A}^- = e^{+i\phi_2}T^+ + P^+, \tag{D25}$$

$$\overline{A}^0 = e^{+i\phi_2}T^0 - \tfrac{1}{2}(P^+ + P^-), \tag{D26}$$

$$\sqrt{2}A^{-0} = e^{+i\phi_2}T^{+0} + P^+ - P^-, \tag{D27}$$

$$\sqrt{2}A^{0-} = e^{+i\phi_2}(T^+ + T^- + 2T^0 - T^{+0}) - P^+ + P^-, \tag{D28}$$

where the overall phase is fixed with the convention $\text{Im}T^+ = 0$. Thus, there are six complex amplitudes, T^+, T^-, T^0, P^+, P^-, and T^{+0}, corresponding to 11 degrees of freedom; and ϕ_2, corresponding to 12 degrees of freedom in total. This parametrization automatically satisfies the isospin relations without loss of generality; i.e., the isospin relations are the only assumption here.

b. Geometric parametrization

We can parametrize the amplitudes using the geometric arrangement of Fig. 13 that satisfies the isospin relation of
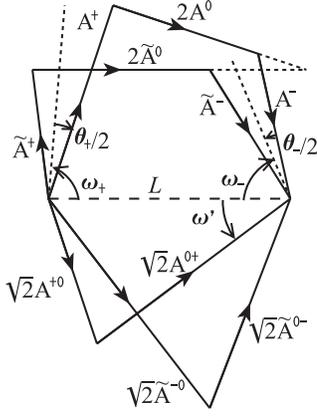
FIG. 13.   Complex pentagons formed from the $B \to \rho\pi$ decay amplitudes.

Eq. (D16). This figure is equivalent to Fig. 3 of Ref. [8], except that the sides corresponding to $B^0 \to \rho^-\pi^+$ and $B^0 \to \rho^0\pi^0$ are swapped. This difference is not physically significant. We apply this modification only to obtain a better behaved parametrization; the parametrization here uses the angles ω_- and θ_- related to the process $B^0(\overline{B}^0) \to \rho^-\pi^+$, which are better behaved than those related to $B^0(\overline{B}^0) \to \rho^0\pi^0$.

To parametrize the amplitudes, we use ϕ_2 and the following 11 geometric parameters:

$$\omega_+, \omega_-, \omega', \theta_+, \theta_-, b_+, b_-, b', a_+, a_-, L, \qquad \text{(D29)}$$

where b and a *imply* branching fraction and asymmetry, respectively. In terms of these parameters, the amplitudes can be described as follows:

$$A^+ = e^{i(\omega_+ + \theta_+/2)}\sqrt{b_+(1 - a_+)/2}, \qquad \text{(D30)}$$

$$\tilde{A}^+ = e^{i(\omega_+ - \theta_+/2)}\sqrt{b_+(1 + a_+)/2}, \qquad \text{(D31)}$$

$$A^- = e^{i(\omega_- + \theta_-/2)}\sqrt{b_-(1 - a_-)/2}, \qquad \text{(D32)}$$

$$\tilde{A}^- = e^{i(\omega_- - \theta_-/2)}\sqrt{b_-(1 + a_-)/2}, \qquad \text{(D33)}$$

$$A^0 = (L - A^+ - A^-)/2, \qquad \text{(D34)}$$

$$\tilde{A}^0 = (L - \tilde{A}^+ - \tilde{A}^-)/2, \qquad \text{(D35)}$$

$$A^{0+} = e^{i\omega'}\sqrt{b'/2}, \qquad \text{(D36)}$$

$$A^{+0} = \frac{L}{\sqrt{2}} - A^{0+}, \qquad \text{(D37)}$$

$$\tilde{A}^{-0} = \frac{L}{\sqrt{2}} - \tilde{A}^{0-}, \qquad \text{(D38)}$$

and

$$\tilde{A}^{0-} = \frac{L}{2\sqrt{2}} - [A^{+0} - A^{0+} - \sqrt{2}(A^+ - A^-)$$
$$+ \sqrt{2}(\tilde{A}^- - \tilde{A}^+)]/2. \qquad \text{(D39)}$$

Equation (D39) exploits the isospin relation of Eq. (D17), which Fig. 13 does not incorporate geometrically. The phase ϕ_2 enters when the $\tilde{A}$'s are converted into $\overline{A}$'s with Eq. (D18). When we perform the analysis only with the time-dependent Dalitz plot observables and without the information from charged decay modes, we remove the parameters ω' and b' from the fit and fix L to be a constant.

This geometric parametrization has a substantial advantage in terms of required computational resources, compared to the parametrization based on the T and P amplitudes described in the previous section. In the procedure to constrain ϕ_2, the minimum χ^2 has to be calculated for each value of ϕ_2. To avoid local minima, initial values of the parameters in the minimization have to be scanned. This inflates the computing time, which increases exponentially with the number of parameters. However, the number of parameters to be scanned decreases in the geometric parametrization. Among the 11 parameters except for ϕ_2, five of them, b_+, b_-, b', a_+, and a_-, are related to the branching fractions and asymmetries. Since in most cases they do not have multiple solutions, we do not have to scan their initial values. In addition, the optimum initial value for L can also be determined using other parameters and b_0, the nominal branching fraction of $B^0 \to \rho^0\pi^0$, from the following relation,

$$b_0 = \left| L - e^{i\omega_+}\sqrt{b_+/2} - e^{i\omega_-}\sqrt{b_-/2} \right|^2, \qquad \text{(D40)}$$

up to a twofold ambiguity. Here b_0 is calculated using the input parameters as

$$b_0 = \frac{U_0^+}{U_+^+ + U_-^+} \cdot \frac{\mathcal{B}(\rho^\pm\pi^\mp)}{c \cdot \tau_{B^0}}, \qquad \text{(D41)}$$

based on Eqs. (22) and (D11). The explicit solution for the optimal initial value of L is

$$L = \text{Re}\gamma \pm \sqrt{b_0 - (\text{Im}\gamma)^2}$$
$$\left(\text{where } \gamma \equiv e^{i\omega_+}\sqrt{b_+/2} + e^{i\omega_-}\sqrt{b_-/2}\right). \qquad \text{(D42)}$$

When $b_0 - (\text{Im}\gamma)^2 < 0$, there is no real-valued solution and $L = \text{Re}\gamma$ is the optimum initial value. With the optimum values calculated above, the initial value of L does not have to be scanned, except for the twofold ambiguity. Consequently, the number of parameters to be scanned in this parametrization is only five, corresponding to ω_+, ω_-, ω', θ_+, and θ_-, while 10 of the 11 parameters have to be scanned in the T and P amplitude parametrization. This leads to a substantial reduction of the computational resources required.

[1] M. Kobayashi and T. Maskawa, Prog. Theor. Phys. **49**, 652 (1973).

[2] A. B. Carter and A. I. Sanda, Phys. Rev. Lett. **45**, 952 (1980).

[3] A. B. Carter and A. I. Sanda, Phys. Rev. D **23**, 1567 (1981).

[4] I. I. Y. Bigi and A. I. Sanda, Nucl. Phys. **B193**, 85 (1981).

[5] Throughout this paper, the inclusion of the charge conjugate decay mode is implied unless otherwise stated.

[6] A. E. Snyder and H. R. Quinn, Phys. Rev. D **48**, 2139 (1993).

[7] H. J. Lipkin, Y. Nir, H. R. Quinn, and A. E. Snyder, Phys. Rev. D **44**, 1454 (1991).

[8] M. Gronau, Phys. Lett. B **265**, 389 (1991).

[9] A. Kusaka *et al.* (Belle Collaboration), Phys. Rev. Lett. **98**, 221602 (2007).

[10] B. Aubert *et al.* (*BABAR* Collaboration), Phys. Rev. D **76**, 012004 (2007).

[11] B. Aubert *et al.* (*BABAR* Collaboration), Phys. Rev. D **72**, 052002 (2005).

[12] S. Kurokawa and E. Kikutani, Nucl. Instrum. Methods Phys. Res., Sect. A **499**, 1 (2003), and other papers included in this volume.

[13] A. Abashian *et al.* (Belle Collaboration), Nucl. Instrum. Methods Phys. Res., Sect. A **479**, 117 (2002).

[14] Z. Natkaniec *et al.* (Belle SVD2 Group), Nucl. Instrum. Methods Phys. Res., Sect. A **560**, 1 (2006).

[15] Strictly speaking, the difference between the $\pi^{\pm}$ and π^0 masses is taken into account, and thus the form factors $F_{\pi}(s_{\pm})$ and $F_{\pi}(s_0)$ are slightly different. The essential point here is, however, that one unique set of (β, γ) is used for all six $\overset{(-)}{F}{}^{\kappa}_{\pi}$.

[16] G. J. Gounaris and J. J. Sakurai, Phys. Rev. Lett. **21**, 244 (1968).

[17] Though there are resonance models other than the GS model that we adopted here, the possible uncertainty due to model dependence is negligibly small compared to the other systematic error sources related to the line shape. This is because the linear combination using the GS model reproduces well the resonant shapes of the experimental data taken on the ρ resonances [18–20], which have much higher statistics than ours. However, the model dependence needs to be addressed in future analyses with much higher statistics. Indeed, there are theoretical complications such as possible unitarity violation in modeling the overlapping broad resonances as a linear combination of Breit-Wigner shapes [21].

[18] S. Anderson *et al.* (CLEO Collaboration), Phys. Rev. D **61**, 112002 (2000).

[19] R. R. Akhmetshin *et al.* (CMD-2 Collaboration), Phys. Lett. B **527**, 161 (2002).

[20] S. Schael *et al.* (ALEPH Collaboration), Phys. Rep. **421**, 191 (2005).

[21] W. M. Yao *et al.* (Particle Data Group), J. Phys. G **33**, 713 (2006), the review *Dalitz plot analysis formalism*.

[22] H. R. Quinn and J. P. Silva, Phys. Rev. D **62**, 054002 (2000).

[23] H. Tajima *et al.*, Nucl. Instrum. Methods Phys. Res., Sect. A **533**, 370 (2004).

[24] H. Kakuno *et al.*, Nucl. Instrum. Methods Phys. Res., Sect. A **533**, 516 (2004).

[25] K. Abe *et al.* (Belle Collaboration), Phys. Rev. D **71**, 072003 (2005).

[26] K. F. Chen *et al.* (Belle Collaboration), Phys. Rev. D **72**, 012004 (2005).

[27] H. Albrecht *et al.* (ARGUS Collaboration), Phys. Lett. B **241**, 278 (1990).

[28] S. Eidelman *et al.* (Particle Data Group), Phys. Lett. B **592**, 1 (2004), and 2005 partial update (http://pdg.lbl.gov).

[29] J. Dragic *et al.* (Belle Collaboration), Phys. Rev. D **73**, 111105 (2006).

[30] Heavy Flavor Averaging Group (HFAG), arXiv:hep-ex/0603003; and online update of Summer 2006 (http://www.slac.stanford.edu/xorg/hfag).

[31] M. Ablikim *et al.* (BES Collaboration), Phys. Lett. B **598**, 149 (2004).

[32] H. Muramatsu *et al.* (CLEO Collaboration), Phys. Rev. Lett. **89**, 251802 (2002).

[33] E. M. Aitala *et al.* (E791 Collaboration), Phys. Rev. Lett. **86**, 770 (2001).

[34] E. M. Aitala *et al.* (E791), Phys. Rev. Lett. **86**, 765 (2001).

[35] K. L. Au, D. Morgan, and M. R. Pennington, Phys. Rev. D **35**, 1633 (1987).

[36] V. V. Anisovich and A. V. Sarantsev, Eur. Phys. J. A **16**, 229 (2003).

[37] O. Long, M. Baak, R. N. Cahn, and D. Kirkby, Phys. Rev. D **68**, 034010 (2003).

[38] C. C. Wang *et al.* (Belle Collaboration), Phys. Rev. Lett. **94**, 121801 (2005).

[39] M. Gronau and J. Zupan, Phys. Rev. D **70**, 074031 (2004).

[40] M. Gronau, E. Lunghi, and D. Wyler, Phys. Lett. B **606**, 95 (2005).

[41] A. Gordon *et al.* (Belle Collaboration), Phys. Lett. B **542**, 183 (2002).

[42] J. Charles *et al.* (CKMfitter Group), Eur. Phys. J. C **41**, 1 (2005).

[43] $\Delta\chi^2(\phi_2)$ is usually expected to follow a χ^2 distribution with 1 degree of freedom, and thus the cumulative χ^2 distribution for 1 degree of freedom is usually used to convert $\Delta\chi^2(\phi_2)$ into a $1 - $ C.L. plot. A toy MC study shows, however, that this is not the case for $B \to \rho\pi$, and an analysis with this assumption yields confidence intervals with undercoverage. Thus, we perform a dedicated toy MC study to obtain the confidence interval.